HIM

Helmholtz-Institut Mainz

All-Optical Room Temperature Magnetic Field Sensing via Electromagnetic Induced Transparency of Nitrogen-Vacancy Centers in Diamond

A REPORT SUBMITTED TO PROF. BUDKER AS THE REPORT OF SUMMER RESEARCH PROGRAM OF NV DIAMOND

2019

Wang Hang

Supervisor: Dr. Geoffrey Iwata

Helmholtz Institute Mainz

Contents

Contents

Abstract

Electromagnetically induced transparency(EIT) is used to probe the narrow electron-spin resonance of nitrogen-vacancy(NV) centers in diamond at low temperature. Its all-optical advantage and promising sensitivity make it a competitive technology for measuring external electric and magnetic fields. However, the low temperature restriction limits its application. Here we analyze the theoretical feasibility and propose an experimental scheme for room temperature EIT in NV centers by using the excited-state level anticrossing.

This report concludes the investigation and the modeling work in August and September. We will first discuss the basic knowledge of electromagnetic induced transparency(EIT). Then we try to cover the background knowledge of NV energy levels and review the previous work of EIT in NV centers at low temperature. Finally we will discuss the level anticrossing(LAC) structure in the NV center and analyse the feasibility of room temperature EIT.

Chapter 1

Introduction

1.1 Preface

Except for the analysis and modeling of room temperature EIT, the report has the following benefits:

If an experimentalist who has basic knowledge of quantum optics wants to do some calculations of EIT, the second chapter should be helpful.

If an experimentalist who has basic knowledge of group representation theory wants to understand the NV center in a deeper physics perspective while not wanting to study the hard theory papers, the third chapters should be helpful.

If one wants to figure out CPT/EIT in the NV center at low temperature, the third chapter should be helpful.

If one wants to figure out the the level anticrossing in the NV center at room temperature, the fourth chapter should be helpful. If one wants to do calculations about this, the fourth chapter should be more helpful.

Besides, all codes for calculation could be find in Codes

1.2   Overview

Laser induced coherence of the atom states could lead to quantum interference between the transition probability amplitudes that modifies optical response of an atomic medium and in this way eliminates the absorption and refraction at the resonant frequency of a transition. This is termed electromagnetically induced transparency(EIT)[1, 2]. EIT results in ultranarrow transmissive spectral features[3] and permits more than 10^7 reduction in optical group velocity[4, 5]. Many EIT-based applications were pursued[6, 7, 8] and its principles are elaborated upon many reviews[9, 10].

Compared with the atomic gases, solid system benefits for compatibility with large-scale fabrication processes. Ensembles of nitrogen-vacancy(NV) centers in diamond exhibit strong NV-light coupling[11] and long spin coherence time(especially in low temperature using dynamic decoupling techniques[12]). The coherent population trapping was observed in NV centers at low temperature more than a decade ago[13, 14] and was recently realized initialization, readout, and unitary manipulation of a single spin[15]. After the early EIT observation in high-defect-density diamond[16], low-defect-density diamond at zero magnetic field was shown to be a promising candidate for all-optical electric and magnetic field sensing with a high sensitivity up to $0.2\text{V/cm}/\sqrt{\text{Hz}}$ and $0.1\text{nT}/\sqrt{\text{Hz}}$[17].

The previous work mainly focus on the application of a Λ system consisting of two ground-state spin sublevels coupled to a spin-composite excited-state sublevel [18] which is restricted by low temperature condition. Here we present the detailed analysis of the Λ structure at room temperature. The sublevels of excited-state at room temperature will have avoided crossings under an axial magnetic field around 500G and therefore could form a three-level Λ structure[19, 20, 21, 22]. Our simplified model shows that there are many difficulties while there is still a glimmer of hope. This report contains

most of the needed background knowledge of both general EIT and the NV center, the discussion of two cases of level anticrossing, and the investigation of diamond-EIT at both low and room temperature.

1.3   Report Structure

The summary of the following contents of this report are presented below.

- **Chapter 2** introduces the underlying physical concepts of EIT through coupling of near resonant laser fields with the states of a 3-level system.

- **Chapter 3** first covers the background knowledge of the NV center from a group theory start, and then introduces several schemes for low temperature coherent population trapping(CPT), finally discusses the low temperature NV EIT.

- **Chapter 4** first introduces basic physics concepts and processes related to the ground states level anticrossing(GSLAC) and excited states level anticrossing(ESLAC), then reproduces the calculation of dynamical nuclear polarization in ESLAC in two ways, analysis the transverse coupling in LAC, and turn to the analysis of the difficulties and the possibility of the room temperature EIT around the excited state level anticrossing(ESLAC).

- **Chapter 5** is the conclusion of the present work and the future plan.

Chapter 2

Introduction to Electromagnetically Induced Transparency

2.1 Effective Hamiltonian

Very often we need to simplify the form of Hamiltonian, one way to do it is unitary transformation[23]. Under a unitary transformation operator U, the Hamiltonian for the system becomes $H' = U^\dagger H U$, and the states are transformed according to $|\psi'\rangle = U^\dagger |\psi\rangle$. After substitution and rearrangement in the Schrodinger equation, we can obtain

$$(H' - iU^\dagger \frac{\partial U}{\partial t})|\psi'\rangle = i\frac{\partial}{\partial t}|\psi'\rangle. \tag{2.1}$$

where we can say the "effective Hamiltonian" H' in the new basis is given by

$$\widetilde{H} = U^\dagger H U - iU^\dagger \frac{\partial U}{\partial t}. \tag{2.2}$$

We now generalize the unitary transformation to density matrix[24] form. Assuming that unitary matrix satisfies the form $U = exp^{-iU_0 t}$, we get $U^\dagger \frac{\partial U}{\partial t} = -\frac{\partial U^\dagger}{\partial t} U$. Then the density matrix in the new basis, $\widetilde{\rho} = U^\dagger \rho U$ will satisfy the time evolution equation,

$$\frac{\partial \widetilde{\rho}}{\partial t} = -i[\widetilde{H}, \widetilde{\rho}]. \tag{2.3}$$

where $\widetilde{H} = U^\dagger H U - iU^\dagger \frac{\partial U}{\partial t}$. The usefulness of unitary transformation will be shown in the following sections. We define the Planck constant $\hbar$ to be 1 in this section.

2.2 Coherent Population Trapping

Before we discuss the dynamics of EIT, we start from coherent population trapping(CPT), known as the creation of a dark coherent superposition of atomic states. We use 'p' and 'c' as labels for the probe and coupling field.
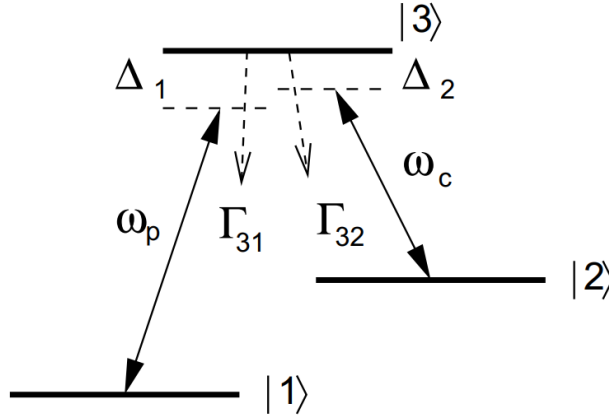

Figure 2.1: Generic system for EIT: Lambda-type scheme with probe field of frequency ω_p and coupling field of frequency ω_c. $\Delta_1 = \omega_{31} - \omega_p$ and $\Delta_2 = \omega_{32} - \omega_c$ denote field detunings from atomic resonances and Γ_{ik} denotes radiative decay rates from state $|i\rangle$ to state $|k\rangle$

The Hamiltonian under rotating-wave approximation to describe the problem

of a three-level atom interacting with a two-mode field is:

$$H = H_0 + H_1, \tag{2.4}$$

where H_1 is the interaction with the light field

$$H_0 = \hbar\omega_1 |1\rangle \langle 1| + \hbar\omega_2 |2\rangle \langle 2| + \hbar\omega_3 |3\rangle \langle 3|, \tag{2.5}$$

$$H_1 = -\hbar \left(\Omega_p e^{-i\phi_p} cos(\omega_p t)|3\rangle \langle 1| + \Omega_c e^{-i\phi_c} cos(\omega_c t)\big| 3\rangle \langle 2|\right) + \text{H.c.} \tag{2.6}$$

We first simplify the Hamiltonian by choosing U as

$$U = \begin{bmatrix} e^{-i\omega_1 t} & 0 & 0 \\ 0 & e^{-i\omega_2 t} & 0 \\ 0 & 0 & e^{-i\omega_3, t} \end{bmatrix}, \tag{2.7}$$

Then according to (2.2) and in the rotating-wave approximation, the Hamiltonian is simplified to (notice $\omega_{31} = \omega_3 - \omega_1, \omega_{32} = \omega_3 - \omega_2$):

$$H_{int} = -\frac{\hbar}{2} \left[\Omega_p(t)|3><1|e^{i\Delta_1 t} + \Omega_c(t)|3><2|e^{i\Delta_2 t} + h.c. \right]. \tag{2.8}$$

This is actually the Hamiltonian in the interaction picture. Now we turn to the useful dressed picture which will be used in the whole report. The term "dressed" could be more understandable in mathematics. We change the unitary matrix (2.7) to

$$U = \begin{bmatrix} 1 & 0 & 0 \\ 0 & e^{-i(\omega_p - \omega_c)t} & 0 \\ 0 & 0 & e^{-i\omega_p t} \end{bmatrix}, \tag{2.9}$$

By (2.2) and (2.9), the new Hamiltonian in the dressed picture is

$$H_{dressed} = -\frac{\hbar}{2} \begin{bmatrix} 0 & 0 & \Omega_p \\ 0 & -2(\Delta_1 - \Delta_2) & \Omega_c \\ \Omega_p & \Omega_c & -2\Delta_1 \end{bmatrix}. \tag{2.10}$$

where $\Delta_1 = \omega_{31} - \omega_p$ and $\Delta_2 = \omega_{32} - \omega_c$. In the two-photon resonance $\Delta_2 = \Delta_1$, the eigenstates can be written in terms of the bare atom states:

$$\left| a^+ \right\rangle = \sin\theta \sin\phi |1\rangle + \cos\phi |3\rangle + \cos\theta \sin\phi |2\rangle, \tag{2.11}$$

$$\left| a^0 \right\rangle = \cos\theta |1\rangle - \sin\theta |2\rangle, \tag{2.12}$$

$$\left| a^- \right\rangle = \sin\theta \cos\phi |1\rangle - \sin\phi |3\rangle + \cos\theta \cos\phi |2\rangle. \tag{2.13}$$

The mixing angles are

$$\tan\theta = \frac{\Omega_p}{\Omega_c}, \tag{2.14}$$

$$\tan 2\phi = \frac{\sqrt{\Omega_p^2 + \Omega_c^2}}{\Delta}. \tag{2.15}$$

$\left| a^0 \right\rangle$ remains at zero energy and $\left| a^+ \right\rangle$ and $\left| a^- \right\rangle$ are shifted up and down by an amount $\hbar\omega^\pm$.

$$\hbar\omega^\pm = \frac{\hbar}{2}(\Delta \pm \sqrt{\Delta^2 + \Omega_p^2 + \Omega_c^2}). \tag{2.16}$$

State $\left| a^0 \right\rangle$ has no component from $|3\rangle$ and is therefore a dark-state since if the atom is formed in this state in the presence of light there is no possibility of excitation to $|3\rangle$ and subsequent spontaneous emission.

A different way to understand CPT[23] is to consider the interaction with $|3\rangle$ of any coherent superposition of states $|1\rangle$ and $|2\rangle$: $|\psi\rangle = a|1\rangle + b|2\rangle$ where a and b are complex coefficients.

The amplitude P for photon absorption in the dipole approximation is

proportional to the product of the dipole transition matrix and the optical electric field, $\vec{d} \cdot \vec{\xi}$. In the present case,

$$P \propto \langle 3|\vec{d} \cdot \vec{\xi}|\psi\rangle = a\langle 3|d|1\rangle \xi_p + b\langle 3|d|2\rangle \xi_c = ad_{31}\xi_p + bd_{32}\xi_c. \qquad (2.17)$$

where ξ_c is the amplitude of the drive field. When

$$b = -\frac{d_{31}\xi_p}{d_{32}\xi_c}a. \qquad (2.18)$$

the amplitude P vanishes and the atoms are in the dark state where they do not interact with light.

2.3 Physics concept of Electromagnetic Induced Transparency

If we choose that $\xi_c >> \xi_p$, then the atoms are always in state $|1\rangle$ (see the final part of section 2.2), with no absorption, this is EIT. If initial state deviates from the dark state, spontaneous emission will pump it finally to the dark state.

In contrast to CPT which is a "spectroscopic" phenomenon that involves only modifications to the material states in an optically thin sample, EIT is a phenomenon specific to optically thick media where both the optical fields and the material states are modified[10]. The destructive interference of EIT could be plainly described in the dressed state. A pair of closely spaced lifetime broadened resonances are equivalent to dressed states created by coupling a pair of well separated atomic bound levels with a resonant laser field[25](Fig 2.2). The strong coupling field ξ_c split the two states$|2\rangle$ and $|3\rangle$ in the dressed picture, which bring about two absorption peak, also known

as Autler-Townes(AT)[26] splitting. When the probe light is detuned to the middle of two peaks, the excitation passways interfere destructively. The distance between the two peaks approximately follow the formula of AC stark shift. When the intensity of probe light is small enough, the distance between two absorption peaks is $2 * \Omega_c/2$. When taking the probe light into consideration, it should be modified to $2 * \sqrt{\Omega_c^2 + \Omega_p^2}/2$. Above will soon be proven in the quantitative calculation later.
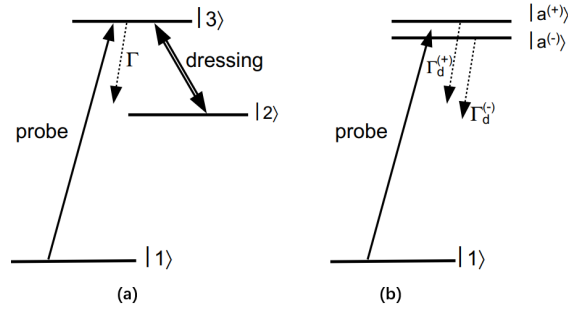

Figure 2.2: Coherent coupling of $|2\rangle$ to $|3\rangle$ (left) generates interference of excitation pathways through the doublet of dressed states $|a^{\pm}\rangle$ (Autler-Townes doublet) provided the decay out of state $|2\rangle$ is negligible as compared to that of state $|3\rangle$[10]

2.4 Analysis of Electromagnetically Induced Transparency

Now we turn to the quantitative calculation of EIT, we do it in the dressed picture. The Hamiltonian is just (2.10), and the steady-state solution for master equation for density matrix is,

$$0 = \frac{\mathrm{d}\rho}{\mathrm{d}t} = \frac{1}{i\hbar}\left[H_{dressed}, \rho\right] + L(\rho). \tag{2.19}$$

The $L(\rho)$ is the Lindblad terms in the master equation[27].

$$
\begin{aligned}
L(\rho) &= \sum_n \gamma_n \left(C_n \rho C_n^\dagger - \frac{1}{2} C_n C_n^\dagger \rho - \frac{1}{2} \rho C_n C_n^\dagger \right) \\
&= \frac{\Gamma_{31}}{2} \left[2\hat{\sigma}_{13}\rho\hat{\sigma}_{31} - \hat{\sigma}_{33}\rho - \rho\hat{\sigma}_{33} \right] + \frac{\Gamma_{32}}{2} \left[2\hat{\sigma}_{23}\rho\hat{\sigma}_{32} - \hat{\sigma}_{33}\rho - \rho\hat{\sigma}_{33} \right] \\
&+ \frac{\gamma_{2deph}}{2} \left[2\hat{\sigma}_{22}\rho\hat{\sigma}_{22} - \hat{\sigma}_{22}\rho - \rho\hat{\sigma}_{22} \right] + \frac{\gamma_{3deph}}{2} \left[2\hat{\sigma}_{33}\rho\hat{\sigma}_{33} - \hat{\sigma}_{33}\rho - \rho\hat{\sigma}_{33} \right].
\end{aligned}
\tag{2.20}
$$

Here we adopt the form in [10], where $\hat{\sigma}_{ij} = |i\rangle\langle j|$ is the atomic projection operator (i, j = 1, 2, 3), Γ_{31} and Γ_{32} is the spontaneous emission and γ_{3deph} and γ_{2deph} describe energy conserving dephasing process.

The form of Hamiltonian will be modified by the unitary transformation, while the form of Lindblad equation is immutable under unitary transformation. So the mathematical form of $L(\rho)$ is then same in Schrödinger picture, interaction picture and the dressed picture.

Assuming all N_{atom} atoms contained in the volume V couple identically to the electromagnetic fields, we let $\varrho = N_{atom}/V$ and setting the input light polarized in the z direction with $\boldsymbol{\mu}_{13} = \mu_{13}\hat{\boldsymbol{z}}$ and $\boldsymbol{\mu}_{23} = \mu_{23}\hat{\boldsymbol{z}}$, we obtain the the expectation value of the atomic polarization

$$
P(t) = \varrho \left[\mu_{13}\rho_{31}e^{-i\omega_p t} + \mu_{23}\rho_{32}e^{-i\omega_c t} + c.c. \right].
\tag{2.21}
$$

Therefore, the linear susceptibility $\chi^{(1)}\left(-\omega_p, \omega_p\right)$ is[10]

$$
\begin{aligned}
\chi^{(1)}\left(-\omega_p, \omega_p\right) = &\frac{|\mu_{13}|^2 \varrho}{\epsilon_0 \hbar} \times \Big[\frac{4\delta\left(|\Omega_c|^2 - 4\delta\Delta\right) - 4\Delta\gamma_{21}^2}{\| \Omega_c \|^2 + (\gamma_{31} + i2\Delta)(\gamma_{21} + i2\delta)|^2} \\
&+ i \frac{8\delta^2\gamma_{31} + 2\gamma_{21}\left(|\Omega_c|^2 + \gamma_{21}\gamma_{31}\right)}{\| \Omega_c \|^2 + (\gamma_{31} + i2\Delta)(\gamma_{21} + i2\delta)|^2} \Big].
\end{aligned}
\tag{2.22}
$$

where $\gamma_{31} = \Gamma_3 + \gamma_{3deph}$, $\gamma_{31} = \Gamma_3 + \gamma_{3deph}$, $\gamma_{21} = \gamma_{2deph}$, $\Gamma_3 = \Gamma_{31} + \Gamma_{32}$,

$\Delta = \Delta_1$, $\delta = \Delta_1 - \Delta_2$.

Now we analyze the position and width of the absorption peaks(Autler-Townes splitting). Here we consider the simplified model which will be a little different than the actual result in EIT experiments.

For simplification, we neglect the γ_{2deph} and γ_{3deph} whose effect is very similar to the spontaneous decay rate and could just be added to the decay rate, and set $\Gamma_{32} = \Gamma_{31} = \Gamma$. Then the solution of ρ_{31} is

$$\rho_{31} =$$
$$\frac{\Omega_c^2 \left(16a^4 + 16a^2\Gamma^2 - 8a^2\Omega_c^2 + \Omega_c^4 + 4a^2\Omega_p^2 + 2\Omega_c^2\Omega_p^2 + \Omega_p^4\right)}{16a^4\Omega_c^2 + 16a^2\Gamma^2\Omega_c^2 - 8a^2\Omega_c^4 + \Omega_c^6 + 16a^2\Gamma^2\Omega_p^2 + 16a^2\Omega_c^2\Omega_p^2 + 3\Omega_c^4\Omega_p^2 + 3\Omega_c^2\Omega_p^4 + \Omega_p^6}.$$
$$(2.23)$$

By simple mathematical calculation, under $\Omega_p << \Omega_c, \Omega_p << \Gamma$, we obtain that the position of the peaks are $\pm\Omega_c/2$, the width of the peaks are Γ, the height of the peaks are $\Omega_p/(2*\Gamma)$. One thing need to mention is that then the absorption peak is not actually symmetric, this only approximately happens when $\Omega_c >> \Gamma$. Some results are shown in Fig 2.3, here ρ_{13} actually refers to $-Im(\rho_{13})$, and this simplication will be used in the whole report.

In above conditions, the solution for ρ_{33} is,

$$\rho_{33} =$$
$$\frac{8a^2\Omega_c^2\Omega_p^2}{16a^4\Omega_c^2 + 16a^2\Gamma_{32}^2\Omega_c^2 - 8a^2\Omega_c^4 + \Omega_c^5 + 16a^2\Gamma_{32}^2\Omega_p^2 + 16a^2\Omega_c^2\Omega_p^2 + 3\Omega_c^4\Omega_p^2 + 3\Omega_c^2\Omega_p^4 + \Omega_p^6}.$$
$$(2.24)$$

So it has the same properties as ρ_{13}.

However, in actually experiments, we often need to consider the relaxation between the ground states, so we introduce the term Γ_{12} in the master

equation. The new $L^{'}(\rho)$ become

$$L^{'}(\rho) = L(\rho) + \frac{\gamma_{12}}{2}\left[2\hat{\sigma}_{12}\rho\hat{\sigma}_{21} - \hat{\sigma}_{22}\rho - \rho\hat{\sigma}_{22}\right] + \frac{\gamma_{12}}{2}\left[2\hat{\sigma}_{21}\rho\hat{\sigma}_{12} - \hat{\sigma}_{11}\rho - \rho\hat{\sigma}_{11}\right].$$
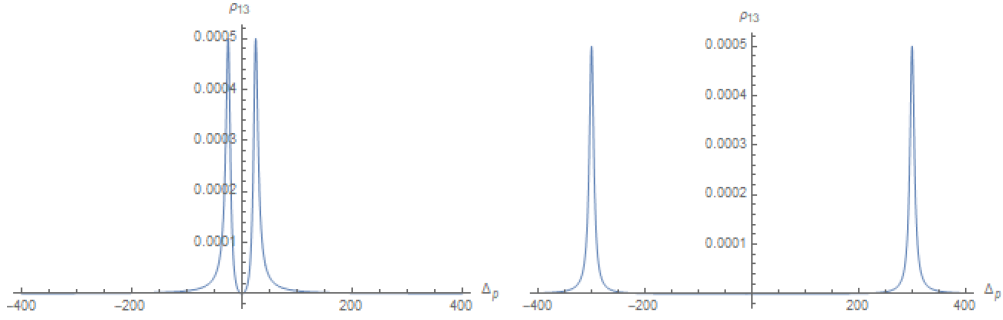
$$(2.25)$$

Figure 2.3: Parameters: $\Gamma = 10$, $\Delta_2 = 0$, $\Omega_p = 0.01, \Omega_c = 50$, $\gamma_{2deph} = \gamma_{3deph} = 0$

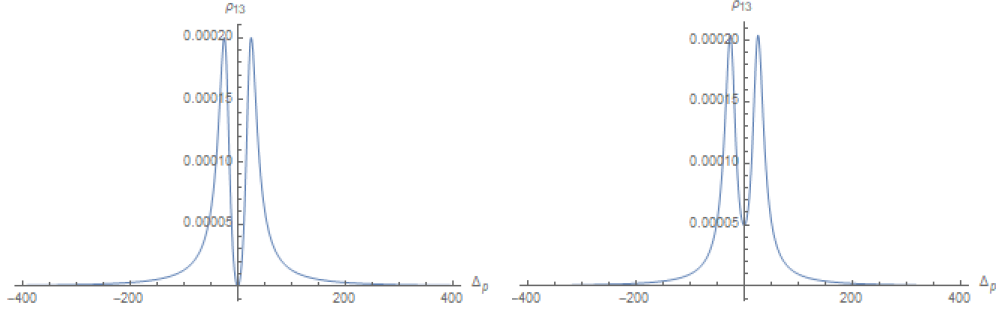Parameters: $\Gamma = 10$, $\Delta_2 = 0$, $\Omega_p = 0.01, \Omega_c = 600, \gamma_{2deph} = \gamma_{3deph} = 0$

Figure 2.4: Parameters: $\Gamma = 25$, $\Delta_2 = 0$, $\Omega_p = 0.01, \Omega_c = 50$, $\gamma_{2deph} = \gamma_{3deph} = 0$

Parameters: $\Gamma = 10$, $\Delta_2 = 0$, $\Omega_p = 0.01, \Omega_c = 50, \gamma_{2deph} = \gamma_{3deph} = 15$

The relaxation will result the difference between ρ_{13} and ρ_{33}, as shown below. And this should be the reason why the previous low temperature EIT paper use ρ_{33} instead of ρ_{13} to calculate the absorption($\Delta_2 = 0$).
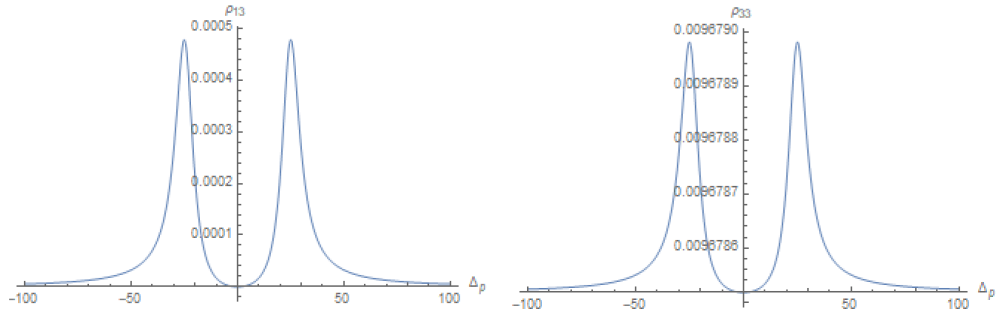
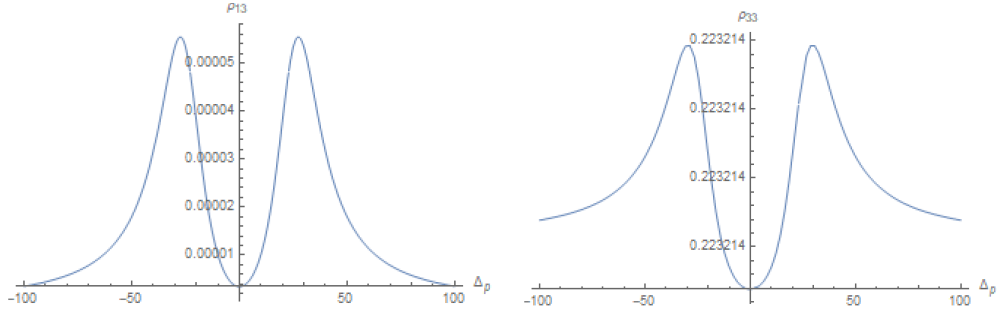Figure 2.5: Para: $\Gamma = 10, \Gamma_{12} = 0.1, \quad \Omega_p = 0.01, \Omega_c = 50, \gamma_{2,3deph} = 0$

Figure 2.6: Para: $\Gamma = 10, \Gamma_{12} = 10, \quad \Omega_p = 0.01, \Omega_c = 50, \gamma_{2,3deph} = 0$

Chapter 3

Electromagnetically Induced Transparency in NV centers at low temperature

3.1   Energy levels in NV center

The NV centre is a point defect in diamond with C_{3v} symmetry consisting of a substitutional nitrogen-lattice vacancy pair orientated along the [111] crystalline direction[28]. In the chemical bonding picture, NV^- contains six electrons, five of which were attributed to C and N atoms surrounding the vacancy while the sixth electron that constituted the formation of negative charge state was assumed to have been accepted from a nearby donor[29],[30]. There are many theoretical researches analyzing and predicting the main properties of the negatively charged NV center in diamond[31],[32],[33],[34]. Here we use group theory approach to derive all the energy levels in NV centers and explain its physical properties[31].

The vacancy in the NV center makes three C and one N atom not have

enough immediate neighbor atoms to form a covalent bond for each of their valence electrons. These unpaired electrons are called *'dangling bonds'*. The NV center obeys C_{3v} symmetry so its single electron orbitals could be classified by the irreducible representation of C_{3v} symmetry. The one-dimensional representation will correspond to a non-degenerate basis and a N-dimensional representation will correspond to a N fold degenerate basis. According to the Burnside theorem, the quadratic sum of the dimension of the non-equivalent irreducible representation is the order of the group (number of elements). The C_{3v} group has 6 elements and $6 = 1^2 + 1^2 + 2^2$. So its irreducible representation consists of two one-dimension representations and a two-dimension representation. The elements of the irreducible representation is shown in Table 1.

C_{3v}	E	C_3^+	C_3^-	σ_d	σ_e	σ_f
A_1	1	1	1	1	1	1
A_2	1	1	1	-1	-1	-1
E	$\begin{pmatrix} 1 & 0 \\ 0 & 1 \end{pmatrix}$	$\begin{pmatrix} \frac{-1}{2} & \frac{-\sqrt{3}}{2} \\ \frac{\sqrt{3}}{2} & \frac{-1}{2} \end{pmatrix}$	$\begin{pmatrix} \frac{-1}{2} & \frac{\sqrt{3}}{2} \\ \frac{-\sqrt{3}}{2} & \frac{-1}{2} \end{pmatrix}$	$\begin{pmatrix} 1 & 0 \\ 0 & -1 \end{pmatrix}$	$\begin{pmatrix} \frac{-1}{2} & \frac{-\sqrt{3}}{2} \\ \frac{-\sqrt{3}}{2} & \frac{1}{2} \end{pmatrix}$	$\begin{pmatrix} \frac{-1}{2} & \frac{\sqrt{3}}{2} \\ \frac{\sqrt{3}}{2} & \frac{1}{2} \end{pmatrix}$

Table1: Irreducible representation of the group C_{3v}

C_{3v}	E	$2C_3$	$3\sigma_v$	$\bar{E}$	$2\bar{C}_3$	$3\bar{\sigma}_v$
A_1	1	1	1	1	1	1
A_2	1	1	−1	1	1	−1
E	2	−1	0	2	−1	0
$E_{1/2}$	2	1	0	−2	−1	0
$^1E_{3/2}$	1	−1	i	−1	1	−i
$^2E_{3/2}$	1	−1	−i	−1	1	i

Table2: Character table of the double C_{3v} group

In the presence of the vacancy, there are four unpaired covalent bonds corresponding to the wave functions $\sigma_1, \sigma_2, \sigma_3, \sigma_N$ where $\sigma_1, \sigma_2, \sigma_3$ are the unpaired bonds for C atoms and σ_N for N atom. Using projective operator, we can use the particular combination of dangling bonds to form the single electron orbitals:

$$\varphi_r = P^{(r)}\sigma_i = \frac{l_r}{h}\sum_e \chi_e^{(r)} R_e \sigma_i. \tag{3.1}$$

where P^r is the projective operator to the irreducible representation(IR) r, $\chi_e^{(r)}$ is the character of operation R_e (element) for the IR r, l_r is the dimension of the IR r, and h is the order of the group. Applying equation (3.1) to the NV center leads to the following combination of σ_S: $\{a_C = (\sigma_1 + \sigma_2 + \sigma_3)/3, e_x = (2\sigma_1 - \sigma_2 - \sigma_3)/\sqrt{6}, e_y = (\sigma_2 - \sigma_3)\sqrt{2}, a_N = \sigma_N\}$. The electron-ion interaction mix orbitals and leads to the single electron orbital basis: $\{a_1(1) = \alpha a_c + \beta a_n, a_1(2) = \alpha a_n + \beta a_c, e_x = (2\sigma_1 - \sigma_2 - \sigma_3)/\sqrt{6}, e_y = (\sigma_2 - \sigma_3)/\sqrt{2}\}$, where α and β are decided by the interaction. The nondegenerate orbitals $a_1(1)$ and $a_2(1)$ are totally symmetric and transform according to the one-dimensional (1D) IR A_1; meanwhile, e_x, e_y are two degenerate states that transform according to the 2D IR E. The ordering of the states is(in the increasing order): $a_1(1)$, $a_1(2)$ and e_x, e_y.

The dynamics of the center are set by the number of electrons available to occupy the orbitals. The ground state configuration consists of four electrons occupying the totally symmetric states and the remaining two electrons pairing up in the e_x, e_y orbitals. In this single particle picture, the excited state configuration can be approximated as one electron being promoted from the $a_1(2)$ orbital to the $e_{x,y}$ orbitals. The orbital description of NV states is very helpful when understanding the charge conversion process(Fig 3.1)[35].

As a filled shell contains 8 electrons, the electronic configuration of this defect can be modeled by two holes occupying the orbitals $e_{x,y}$ in the ground

state (e^2 electronic configuration), one hole each in the orbitals $a_1(2)$ and $e_{x,y}$ for the excited state (ae electronic configuration) and two holes in the orbital $a_1(2)(a^2$ electronic configuration).
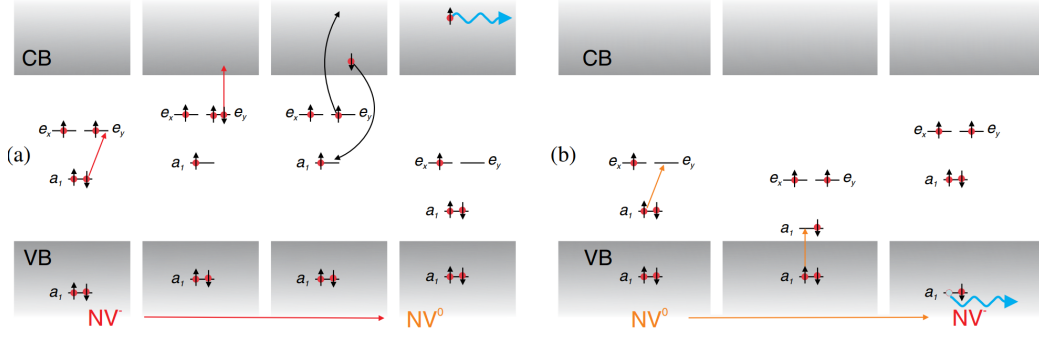

Figure 3.1: Schematic picture of the charge conversion process for negative and neutral states of the NV defect. (a) NV^- to NV^0 conversion involves two photons and an Auger process that releases enough energy to detach an electron from the defect. (b) NV^- recovering occurs in two steps: first, an electron is excited from the a_1 to the e orbital and then an additional electron is transferred form the deep lying a_1 orbital to the vacant place on the a1 orbital in the band gap. The deep hole migrates away from the NV center leaving it in the negative charge state. The position of defect levels changes upon different occupation of states shown schematically for both processes.

The full representation contains the direct product of each hole representation and its spin representation. By projecting any combination of the two-electron wavefunction onto the IRs of the group(now is the double C_{3v} group, see Table2) as equation(3.2), we obtain the two-hole representation in Table3.

$$\Psi^r = P^{(r)}\varphi_1 \otimes \chi_1 \otimes \varphi_2 \otimes \chi_2 = \frac{l_r}{h}\sum_e \chi_e^{(r)*} R_e\varphi_1 \otimes U_e\chi_1 \otimes R_e\varphi_2 \otimes U_e\chi_2. \quad (3.2)$$

The six states in configuration $ea(T)$ are the well-known six-levels excited states and the three states in configuration $e^2(T)$ are the well-known

Configuration	State	Symmetry
e^2 (T)	$\begin{aligned}&^3A_{2-} =\\ &^3A_{20} = \|e_xe_y - e_ye_x\rangle \otimes \left\{ \begin{array}{c} \|\beta\beta\rangle \\ \|\alpha\beta + \|\beta\alpha\rangle \\ \alpha\alpha\rangle \end{array}\right.\\ &^3A_{2+} = \end{aligned}$	$\begin{aligned}&E_1 + E_2\\ &A_1\\ &E_1 - E_2\end{aligned}$
e^2 (S)	$\left.\begin{array}{l}^1E_1 = \|e_xe_x - e_ye_y\rangle \\ ^1E_2 = \|e_xe_y + e_ye_x\rangle \\ ^1A_1 = \|e_xe_x + e_ye_y\rangle\end{array}\right\} \otimes \|\alpha\beta - \beta\alpha\rangle$	$\begin{aligned}&E_1\\ &E_2\\ &A_1\end{aligned}$
ea (T)	$\begin{aligned}A_1 &= \|E_-\rangle \otimes \|\alpha\alpha\rangle - \|E_+\rangle \otimes \|\beta\beta\rangle\\ A_2 &= \|E_-\rangle \otimes \|\alpha\alpha\rangle + \|E_+\rangle \otimes \|\beta\beta\rangle\\ E_1 &= \|E_-\rangle \otimes \|\beta\beta\rangle - \|E_+\rangle \otimes \|\alpha\alpha\rangle\\ E_2 &= \|E_-\rangle \otimes \|\beta\beta\rangle + \|E_+\rangle \otimes \|\alpha\alpha\rangle\\ E_y &= \|Y\rangle \otimes \|\alpha\beta + \beta\alpha\rangle\\ E_x &= \|X\rangle \otimes \|\alpha\beta + \beta\alpha\rangle\end{aligned}$	$\begin{aligned}&A_1\\ &A_2\\ &E_1\\ &E_2\\ &E_1\\ &E_2\end{aligned}$
ea (S)	$\begin{aligned}^1E_x &= \|a_1e_x + e_xa_1\rangle \otimes \|\alpha\beta - \beta\alpha\rangle\\ ^1E_y &= \|a_1e_y + e_ya_1\rangle \otimes \|\alpha\beta - \beta\alpha\rangle\end{aligned}$	$\begin{aligned}&E_1\\ &E_2\end{aligned}$
$a^2(S)$	$^1A_1 = \|a_1a_1\rangle \otimes \|\alpha\beta - \beta\alpha\rangle$	A_1

Table3: The first column shows the electronic configuration and in parentheses their triplet (T) or singlet (S) character. The third column gives the symmetry of the row of the IR. $\alpha(\beta)$ stands for $\uparrow$ ($\downarrow$) and $E_\pm = |a_1e_\pm - e_\pm a_1\rangle$, where $e_\pm = \mp(e_x \pm ie_y)$, $|X\rangle = (|E_-\rangle - |E_+\rangle)/2$ and $|Y\rangle = (|E_-\rangle + |E_+\rangle)i/2$

three-levels ground states. The three states in $e^2(s)$ are the well known "metastable states" which result in the spin polarization. The doubly excite state(a^2) is not optically accessible in the excitation process of the NV center in experiments[31]. There are indeed some sophisticated MBPT calculation indicating that the infrared transition at about 1.1 eV belongs to the $^1E(ae) \rightarrow^1 A_1(e^2)$ transition[36]. However, this calculation is inconsistant with [37], and is considered unconvincing in [28]. By now, there is no good experimental or theoretical result of the singlet excited states.

The Hamiltonian of the ^3E excited state is given by

$$H = H_0 + H_{so} + H_{ss} + H_{str}, \tag{3.3}$$

The spin-orbit effect takes the following

$$H_{SO} = \sum_k \lambda_{xy} \left(l_k^x s_k^x + l_k^y s_k^y \right) + \lambda_z l_k^z s_k^z, \tag{3.4}$$

where $\lambda_{x,y}(\lambda_z)$ denotes the non-axial (axial) strength of the interaction. The axial part of spin-orbit interaction splits the states as

$$H_{SO} = \lambda_z \left(|A_1\rangle \langle A_1| + |A_2\rangle \langle A_2| - |E_1\rangle \langle E_1| - |E_2\rangle \langle E_2| \right). \tag{3.5}$$

However, in the non-axial part, l^+ and l^- link states of different electronic configurations, while s^+ and s^- link $m_s = 1$ excited states with $^1A_1\,(e^2)$ and link $m_s = 0$ ground states with $^1E_{1,2}\,(e^2)$. Thus, the triplet states are linked with singlets states and results in the non-spin-conserving intersystem circle (with averaging effect, in room temperature the whole system is shown in Fig 3.6[38]). The interaction with the single excited states are suppressed by the large gap that separates different electronic configurations. The spin-spin effect would further splits the excited state manifold and even mixes $E_{x,y}$ and $E_{1,2}$, which was considered a reason for the Λ transitions in [14] by [31]. More details could be found in [31].

At low strain, the optical transitions follow the selection rules in Table 4 [39]. However, the effect of strain could decouple the spatial part from the spin part when it overcomes the spin-orbit interaction(a few GHz). The result is in a particular local, the optical transitions between linearly polarized and the excited states split into two triplets with spatial wavefunctions E_x and E_y. In this situation, the effect of the spin-orbit coupling, the spin-spin

interaction and the local strain are shown in Fig 3.2[40].

Pol	A_1	A_2	E_1	E_2	E_x	E_y
$^3A_{2-}$	$\hat{\sigma}_+$	$\hat{\sigma}_+$	$\hat{\sigma}_-$	$\hat{\sigma}_-$		
$^3A_{20}$					$\hat{y}$	$\hat{x}$
$^3A_{2+}$	$\hat{\sigma}_-$	$\hat{\sigma}_-$	$\hat{\sigma}_+$	$\hat{\sigma}_+$		

Table 4: Polarization relations. Linear polarization are represented by $\hat{x}$ and $\hat{y}$, while circular polarizations are represented by $\hat{\sigma}_\pm = \hat{x} + i\hat{y}$
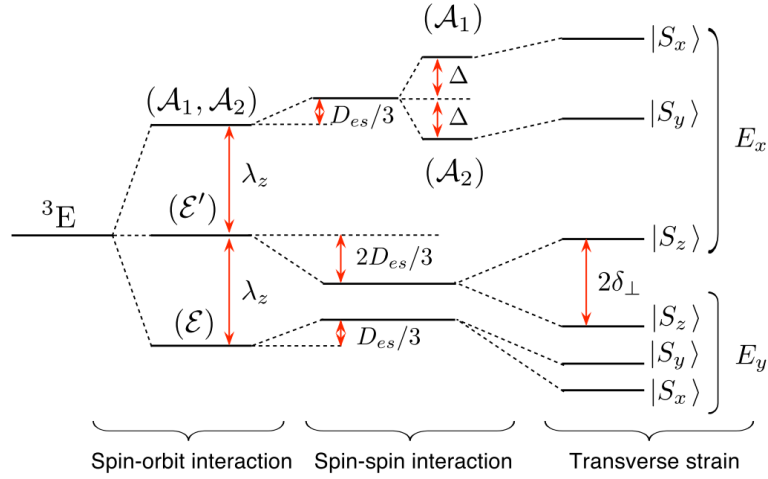
Figure 3.2: Schematic diagram of the excited-state energy levels including spin-orbit interaction, spin-spin interaction and transverse local strain. Note that 1 GPa external stress gives approximately 10^3 GHz splitting)

The effect of strain are shown in Fig 3.3 [39] and we could see that under a particular strain, there is an avoid crossing between $|E_y, S_z\rangle$ and $|E_y, S_x\rangle$ spin sublevels[40], as shown in Fig 3.4.

Lifetime of ^3E is about 12ns and temperature independent[41]. Thus, at higher temperature the larger widths reflects lifetimes of the coupled electron-vibrational system[42]. The averaging quenches the effect of strain, spin-orbit interaction and Δ that splits A_1 and A_2. At sufficiently high temperature, the
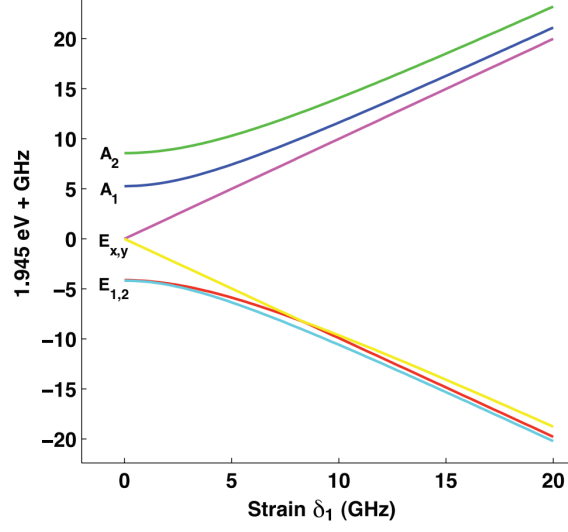
Figure 3.3: Energies of the excited states as a function of strain, expressed in units of the linear strain induced splitting between the $|E_x\rangle$ and $|E_y\rangle$ states
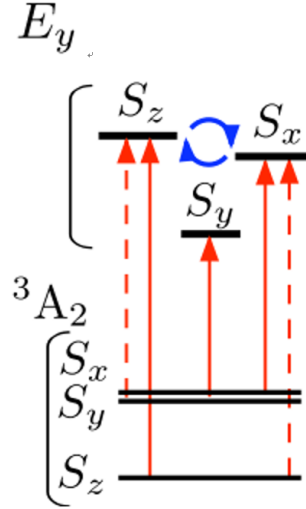

Figure 3.4: Scheme for Spin-flop transitions(dashed line)

phonon transition rates will greatly exceed the ^3E decay rate and the population will be equally distributed between the low temperature fine structure levels of the occupied spin-projection[28]. The result is shown in Fig 3.5[32].

Group theory can also explain why the hyperfine interaction in the excited

states are an order larger than in the ground states, because the ground state wavefunction concentrated in $e_{x,y}$ have no overlap with the nitrogen atom while the orbital $a_1(2)$ is partially localized on the nitrogen atom.
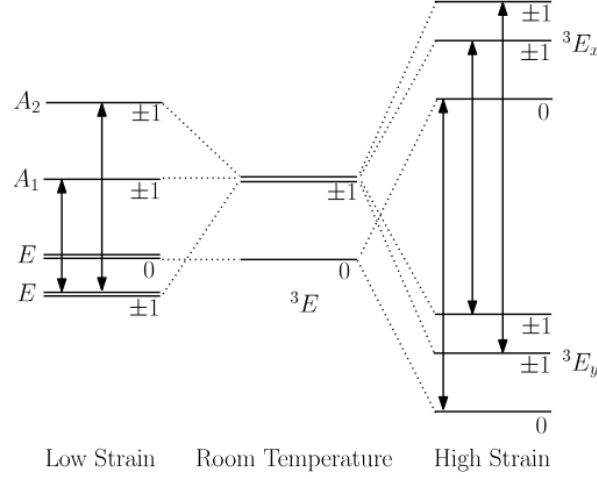
Figure 3.5: Schematic of the observed low temperature ^3E fine structure at low (left) and high (right) strain together with the observed room temperature fine structure (centre)
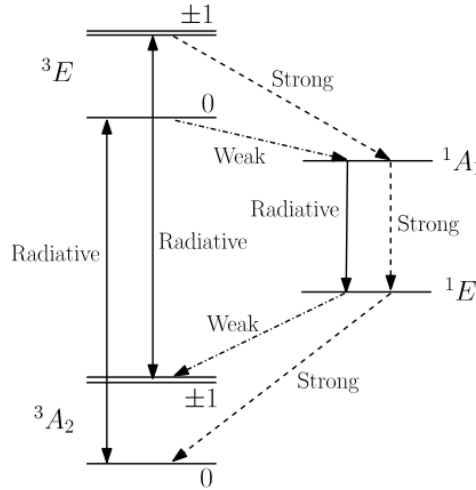

Figure 3.6: Schematic of the NV_- electronic structure including the $^3A_2$ and ^3E (room temperature) fine structure

3.2 Coherent population trapping in NV centers at low temperature

One difference between coherent population trapping(CPT) and EIT is: in EIT, we measure the transmission of the probe beam; while in CPT, a common way is to measure the intensity of photoluminescence (PL). The early work in [13], [14] discussed the CPT using the avoid crossing of excited states at low temperature. A three-level structure was adopted to explain the CPT phenomenon at zero magnetic field in [13] and a four-level structure was adopted in [14].

For the three-level structure, the state $|1\rangle$ represents the $m_s = 0$ ground state, $|2\rangle$ represents a superposition of the $m_s = \pm 1$ states, and $|3\rangle$ represents an excited state. Then the master equation in the steady state is just as equation (2.19), with Hamiltonian of (2.10). The difference is the decoherence and relaxation terms $L[\rho]$ was given phenomenologically.

$$L[\rho] = \begin{pmatrix} \Gamma_{12}\left(\rho_{22} - \rho_{11}\right) + \left(\Gamma_3/2\right)\rho_{33} & -\gamma_{12}\rho_{12} & -\gamma_{13}\rho_{13} \\ -\gamma_{21}\rho_{21} & \Gamma_{12}\left(\rho_{11} - \rho_{22}\right) + \left(\Gamma_3/2\right)\rho_{33} & -\gamma_{23}\rho_{23} \\ -\gamma_{31}\rho_{31} & -\gamma_{32}\rho_{32} & -\Gamma_3\rho_{33} \end{pmatrix}.$$

$$(3.6)$$

where Γ_3 is the total excited-state spontaneous emission rate, Γ_{12} is the transition rate between ground states, and γ_{ij} are the decay rates of the off-diagonal density matrix elements due to pure dephasing and population relaxation, given by $\gamma_{12} = \gamma_{21} = \Gamma_{12} + \gamma_1$ and $\gamma_{13} = \gamma_{31} = \gamma_{23} = \gamma_{32} = \Gamma_{12}/2 + \Gamma_3/2 + \gamma_3$, where γ_1 and γ_3 are parameters for pure dephasing of the ground and excited states, respectively. Above has a subtle difference from the final form of (2.20).

We use Mathematica to reproduce the results of [13] and matches well the

actual modeling which added a linearly sloped background as an additional fitting parameter representing contributions from other subsets of levels. The results in paper are shown in Fig 3.7. Fig 3.8 is the result of reproduction.
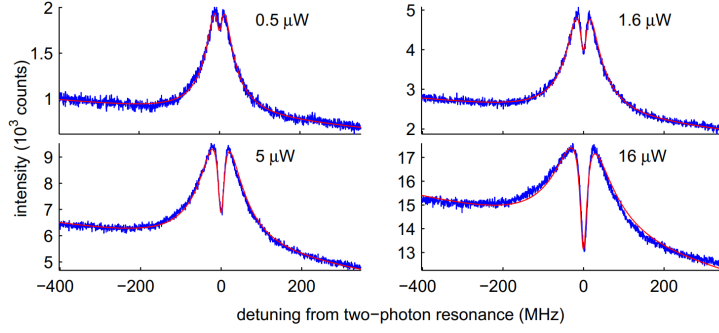

Figure 3.7: Coherent population trapping at various excitation powers. blue:data, red:fit. The indicated powers correspond to both 637nm lasers. For excitation powers 0.5, 1.6, 5, and 16 μW the fits used Rabi frequencies (in this simplified model they are the same for both transitions): 10.1, 14.2, 17.9, and 22.0MHz; effective population decay rates between ground states: 0.11, 0.20, 0.35, and 0.83MHz; excitedstate decoherence: 2.4, 3.0, 6.3, and 11.4MHz; ground-state decoherence: 7.0, 5.8, 3.6, and3.8MHz.
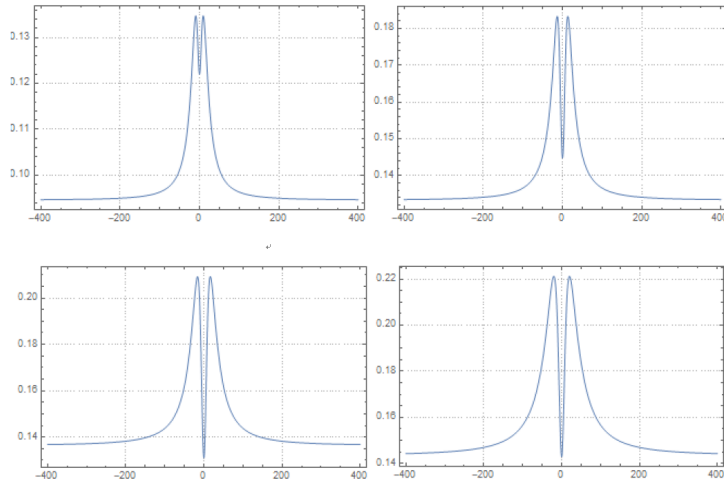

Figure 3.8: Reproduction based on the parameters in Fig 3.7. The actual calculation fit of experiment has an extra linear background which is neglected.

If we consider the case when the magnetic field is not zero. Then we need to use the four-level structure[14]: three ground states $|1\rangle$, $|2\rangle$, $|3\rangle$ represents $m_s = 0$ and two orthogonal linear combinations of $m_s = \pm 1$, and an excited state $|4\rangle$. The Hamiltonian in the rotating frame became

$$\frac{H}{\hbar} = \begin{pmatrix} \delta_1 & 0 & 0 & \Omega_1^*/2 \\ 0 & \delta_2 & 0 & \Omega_2^*/2 \\ 0 & 0 & \delta_2 + \delta_{23} & \Omega_3^*/2 \\ \Omega_1/2 & \Omega_2/2 & \Omega_3/2 & 0 \end{pmatrix}. \tag{3.7}$$

where δ_1 and δ_2 are the laser frequency detunings from the 1-4 and 2-4 transitions, respectively, δ_{23} is the level 2-3 splitting, and Ω_i are the Rabi frequencies proportional to the square root of the laser intensities. Under appropriate decay terms, the theory calculation in [14] matched well with experiments.

Another way to achieve CPT in NV centers is using $|\pm 1\rangle \to |A_2\rangle$ transition (Fig 3.9)[43]. If the state related to the Λ structure is not in the dark state, then it will return back to $|0\rangle$ by optical excitation cycles and intersystem crossing. Thus, if the NV center is not in a dark state, this process effectively increases the number of photons collected by γ_{s1}/γ_{ce}, where γ_{ce} is the cross transition rate from $|E_y\rangle$ into $|\pm 1\rangle$ and γ_{s1} is the rate from $|A_1\rangle$ to the singlet. In [44], nuclear spin states is used to address through their hyperfine coupling to the electron spin of a single nitrogen-vacancy defect as a Λ structure. Also, initialization, readout, and unitary manipulation of a single spin are realized coherent population trapping and stimulated Raman techniques by tuning an NV center to an excited-state spin anticrossing at cryogenic temperatures[45]. These will not be elaborated in the report.
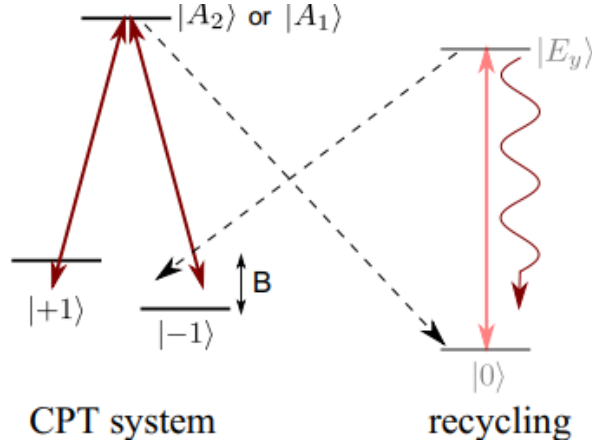
Figure 3.9: The Λ-type transitions between the ground states $|\pm 1\rangle$ and excited states $A_{1,2}$ of a single NV center are addressed with a CPT laser, while a recycling laser drives the $|0\rangle$ to $|E_y\rangle$ transition.

3.3 EIT in NV centers at low temperature

Using the Λ structure in [13], low temperature NV EIT was realized in [17]. We first start from the hyperfine structures at low temperature ground states, which are clearly shown in Fig 3.10[46]. Using multipass configuration to increase the optical path length L, proper sideband:carrier:sideband internsity ratio to optimize contrast(fluorescence from NV centers with allowed spin-flip transitions cannot be observed with a single excitation frequency due to optical pumping), and alternating green and red pulses to minimize bleaching, low temperature EIT in NV centers was realized by [17]. Fig 3.12(c) follows the result shown in Fig 3.10(b) and the values of ν_{EOM} are given by[48], where $g = 2.003$[47].

$$\nu_{i_\pm} = D \pm \sqrt{(g\mu_B B \cos\theta + m_i A_{\mathrm{HF}})^2 + (d_{gs_\perp} E_\perp)^2}. \qquad (3.8)$$

Using the master equation and the Λ structure in 3.2, the data were fitted from the contrast and FWHM as a function of P_{red} at B=0, with decay
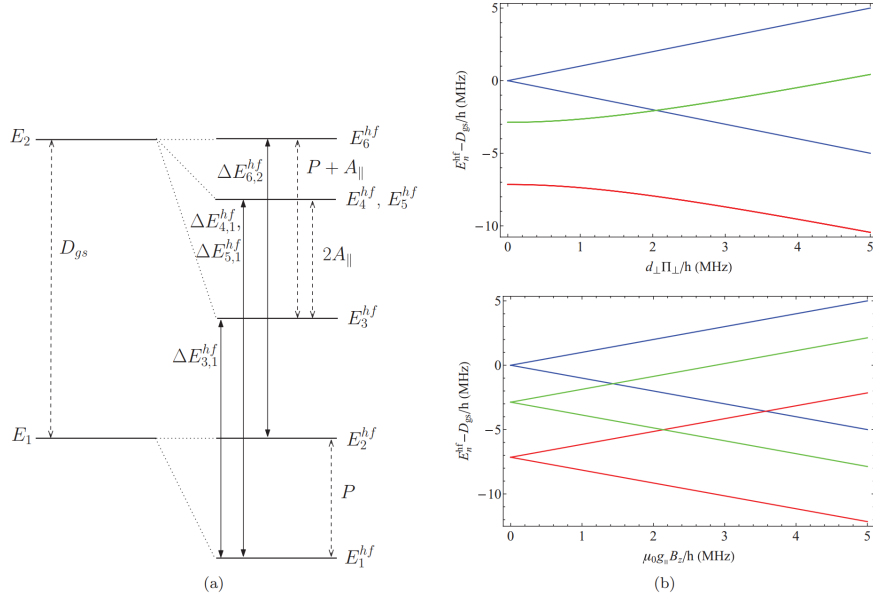
Figure 3.10: (a): The hyperfine structure of the ground triplet. The level splittings are indicated by dashed arrows. The central hyperfine line corresponds to transitions between $m_I = 0$ states and the lower and higher energy lines correspond to transitions between $m_I = \pm 1$ states.(b): The splittings of the $m_s = \pm 1$ hyperfine levels in the presence of nonaxial electric-strain fields of magnitude $\perp$ (upper) and axial magnetic fields Bz (lower). $m_I = 0$ hyperfine levels are colored blue and $m_I = \pm 1$ hyperfine levels are colored red and green. Parameters are from[47]

terms consisting of nuclear-spin-dependent ground-state decoherence γ_{gs,m_i} and longtitudinal ground-state relaxation γ_1. Considering δS as photon shot noise limited, the magnetic sensitivity is given by

$$\delta B_{\min} \simeq \frac{1}{g\mu_B \cos\theta} \frac{\Delta\nu_{\mathrm{EIT}}}{R_1} \sqrt{\frac{E_p}{P t_m}}. \tag{3.9}$$

where P is the detected optical power, E_p is the photon energy, $\Delta\nu_{EIT}$ is the FWHM, R_1 is the zero-field contrast, and t_m is the measurement time. Parameters can be obtained from Lorentizian fitting of Fig 3.12(c). Fig 3.13 is The contrast, FWHM and sensitivity, where these data were fit by a 3-
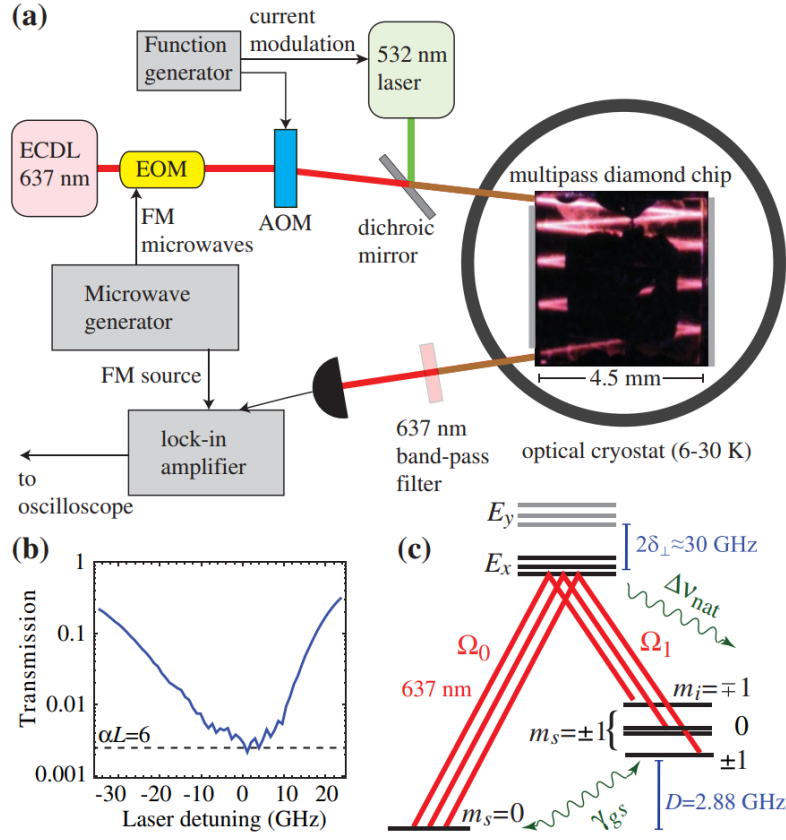
Figure 3.11: (a) Experimental apparatus. Microwave frequency modulation (FM) and lock-in detection were used for magnetometry Acousto-optic modulator, AOM.(b) Transmission spectrum of a weak optical probe. (c) NV level structure and allowed Λ transitions at B = 0 in the moderate-strain regime. ^{14}N quadrupole splitting is omitted

level density-matrix model for EIT in inhomogeneously broadened media. In this fitting, spontaneous emission $\Delta\nu_{nat}$=15 MHz, as well as nuclear-spin-dependent ground-state decoherence γ_{gs,m_i}, and longitudinal ground-state relaxation γ_1 are considered while all other dephasing terms to zero.
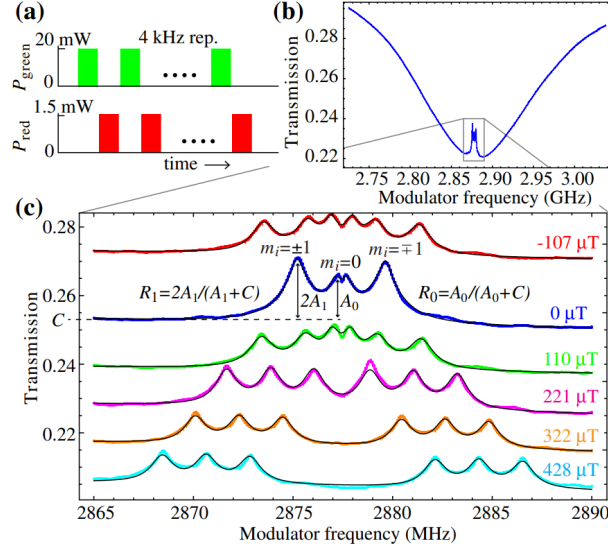
Figure 3.12: (a): Timing diagram of optical pulses used to probe EIT resonances.(b): Transmission spectrum as the sideband-carrier detuning was swept through two-photon resonance. (c): EIT spectra at different magnetic fields applied along a [100] direction. The spectra are offset for clarity. Overlayed are Lorentzian fits.
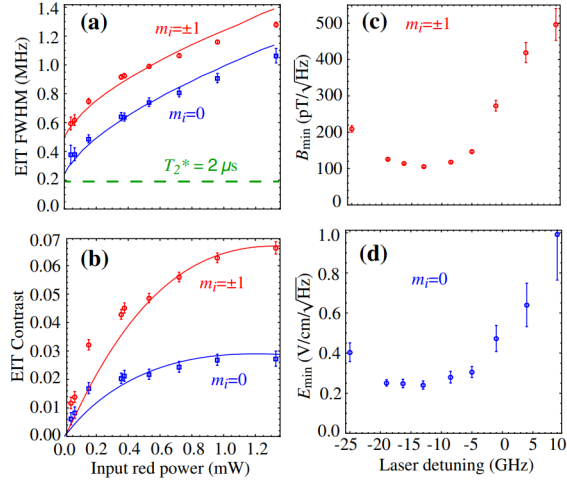

Figure 3.13: (a), (b) Power dependence of zero-field EIT FWHM and contrast determined from Lorentzian fits as in Fig. 3.12(c). (c), (d) Photon-shot-noise-limited magnetic and electric field sensitivity (eq 3.7), inferred from zero-field EIT spectra, as a function of laser detuning.

Chapter 4

Electromagnetically Induced Transparency in NV centers at room temperature

4.1 Ground-state Level Anticrossing

Before we analyze the proposed EIT scheme using ESLAC, we first discuss the underlying physics of the ground-state level anticrossing (GSLAC) which is very similar to ESLAC. There are already many researches on GSLAC. All-optical detection and spectroscopy of externally generated fluctuating magnetic fields at frequencies ranging from 8 MHz down to 500 kHz was realized in ^{14}N[49]. The dynamic nuclear polarization of ^{15}N as a function of magnetic field was modeled in [50]. A theoretical model including the coupling to ^{14}N and ^{13}C was developed in [51]. Also, the application of GSLAC to microwave-free magnetometry was developed in [52], [53].

In beginning, for simplicity, we only consider the interaction with ^{14}N

and neglect all others.

$$\hat{H} = \hat{H}_{\text{el}} + \hat{H}_{\text{14N}} + \hat{H}_{\text{NV+14N}}. \tag{4.1}$$

where $\hat{H}_{\text{el}} = D_g \hat{S}_z^2 + \gamma_e \mathbf{B} \cdot \hat{\mathbf{S}}$, $D_g = 2.87\text{GHz}$, $\hat{H}_{\text{14N}} = Q \hat{I}_z^2 - \gamma_{\text{14N}} \mathbf{B} \cdot \hat{\mathbf{J}}$ and $\hat{H}_{\text{NV+14N}} = \hat{\mathbf{S}} \cdot \hat{A} \cdot \hat{\mathbf{I}}$. The matrix $\hat{A}$ is a diagonal hyperfine-interaction tensor between the electron spin S of the NV center and nuclear spin I of the ^{14}N nucleus that belongs to the NV center.

$$\hat{A} = \begin{pmatrix} A_\perp & 0 & 0 \\ 0 & A_\perp & 0 \\ 0 & 0 & A_\| \end{pmatrix}, \tag{4.2}$$

where $A_\| = -2.14\text{MHz}, A_\perp = -2.70\text{MHz}$. The calculated wavefunctions exhibit avoided crossings shown in Fig 4.1. The accurate mathematical form of wavefunctions could be find in [51] and will not be elaborated here.

The $|m_s = 0, m_I = -1\rangle$ sublevel is mixed with $|m_s = -1, m_I = 0\rangle$ by off diagonal hyperfine coupling terms, after intersystem cycling, it will be spin polarized to $|m_s = 0, m_I = 0\rangle$, then it will be mixed with $|m_s = -1, m_I = 1\rangle$ again by the transverse coupling and finally moves to $|m_s = 0, m_I = 1\rangle$ due to intersystem cycling(we define the magnetic field along the symmetric axis to be "axial"). This can be visually understood in Fig 4.4.

Taking proper Lindblad terms[50], the dynamic nuclear polarization could be calculated, as shown in Fig 4.2(^{15}N the same).

Seemingly, the nuclear spin polarization could be polarized to the maximum in the GSLAC position. However, in [51], the theoretical model mismatched with the ODMR result(similar to the ODMR in 4.2) in the GSLAC position even taking ^{13}C into consideration, and showed that in the GSLAC position, the nuclear spin polarization would decrease, which made
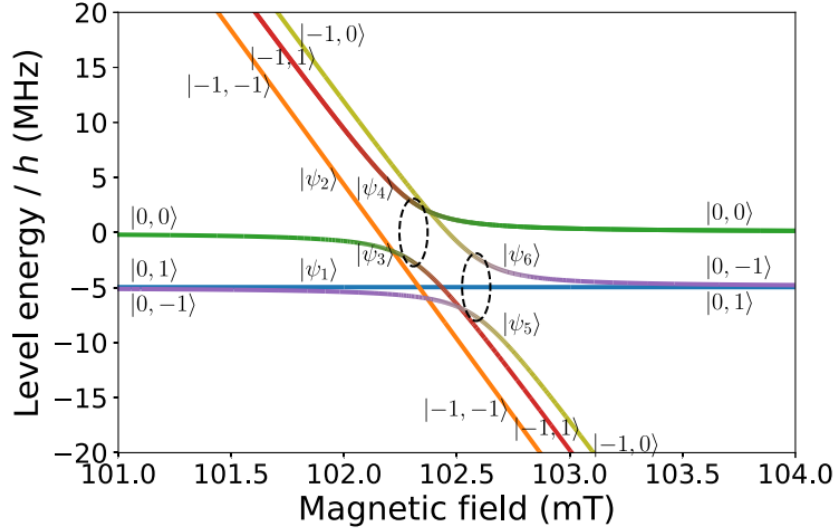
Figure 4.1: Hyperfine level ($|m_S, m_I\rangle$) anticrossing in the vicinity of the GSLAC. The degree of mixing near the GSLAC (denoted by the dashed ellipses) is indicated by the relative admixture of the colors in each curve; the lines corresponding to unmixed states do not change color.

the present understanding of GSLAC problematic.

We guess that the theoretical model of [51] may not be correct, because the calculation is based on the concept of "spin temperature". And one condition for "spin temperature" is that the ensemble average of nuclear spin number is conservative. This is problematic, because the intersystem crossing will violate the conservation of spin momentum, and thus violate the conservation of nuclear momentum.[23], [54]

4.2 Excited-state Level Anticrossing

There are already many studies on ESLAC, most focusing on the dynamic nuclear polarization. In NV centers, it has been demonstrated for ^{14}N [19], [20], [55], ^{13}C [55], [56], [57], ^{15}N [22], [50]. Around 510 G, the transverse hyperfine coupling induces electron-nuclear flipflops, and consequently polarization
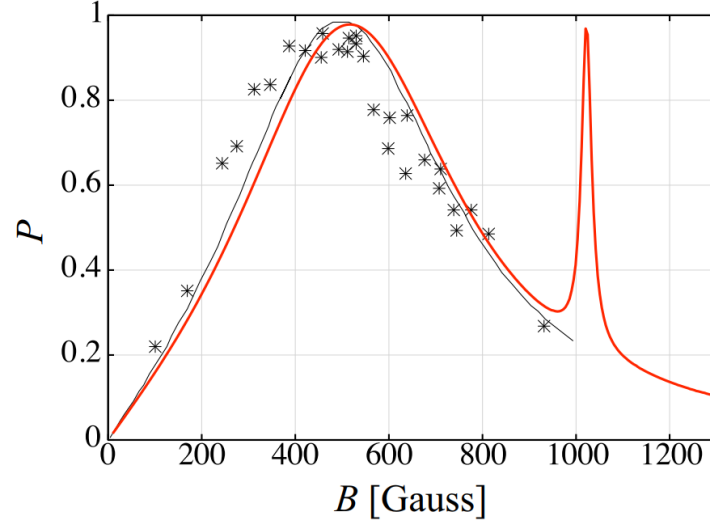
Figure 4.2: A comparison of calculated and measured dynamic nuclear spin polarization P of a ^{15}N nucleus of the NV center in diamond as a function of the external magnetic field B. The result of our calculation is depicted with a thick red solid line, while the previous theoretical and experimental results [22] are depicted with thin black solid line and black points

transfer from electron to nuclear spins. Following the calculation method in [51], we reproduced the hyperfine structure of the excited states(Fig 4.3).
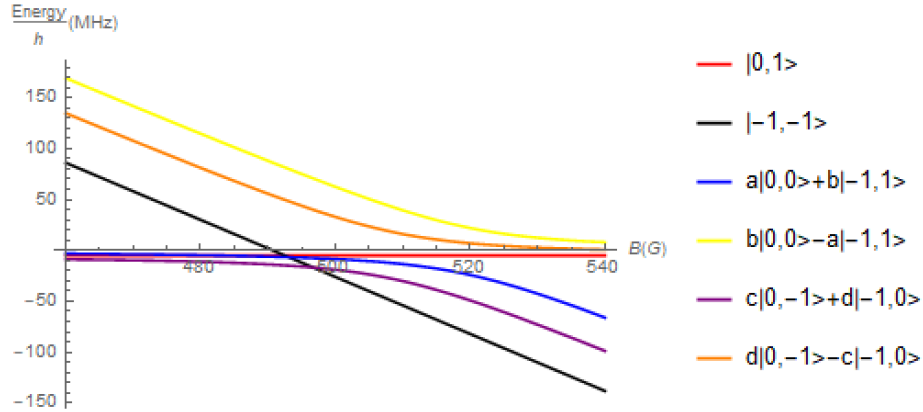

Figure 4.3: Hyperfine energy levels of the excited state

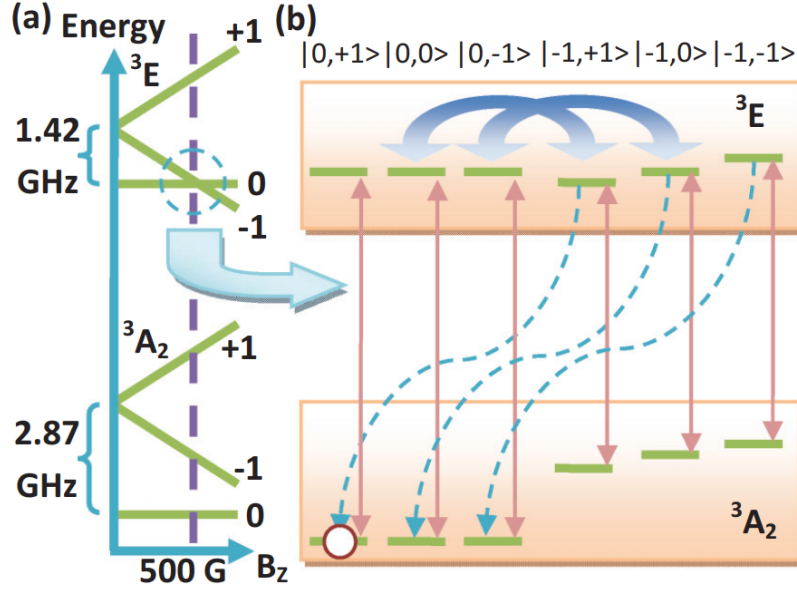The pump process for spin polarization is clearly shown in Fig 4.4 [20].

Figure 4.4: Hyperfine energy levels of the excited state, close to the ESLAC

In order to measure the degree of nuclear polarization, ODMR of $m_s = 0$ to $m_s = 1$ is often conducted. The result of [20] is shown in Fig 4.5. We notice that there is often a small possibility that the NV center will have a coupled C13 nuclear spin.

One thing need to mention is that cross relaxation of the NV center with substitutional nitrogen in the vicinity of the ESLAC decreases the NV's electron polarization, and thus, the nuclear spin polarization as well.[20]

Finally, we reproduce the theoretical calculation of the dynamic nuclear polarization. We first adopt a 9-level model[20] then we extend it to a more complete 21-level model[19]. The Hamiltonian of the excited states is:

$$H_{es} = D_{es}\left(S_Z^2 - \frac{1}{3}\vec{S}^2\right) + E_{es}\left(S_X^2 - S_Y^2\right) + \vec{B}\left(\gamma_{NV}\vec{S} + \gamma_{14N}\vec{I}\right) + \vec{I}\cdot\overline{\overline{A}}\cdot\vec{S} + QI_Z^2$$

(4.3)

We first neglect E_{es} and model the system by solving the steady-state Lind-
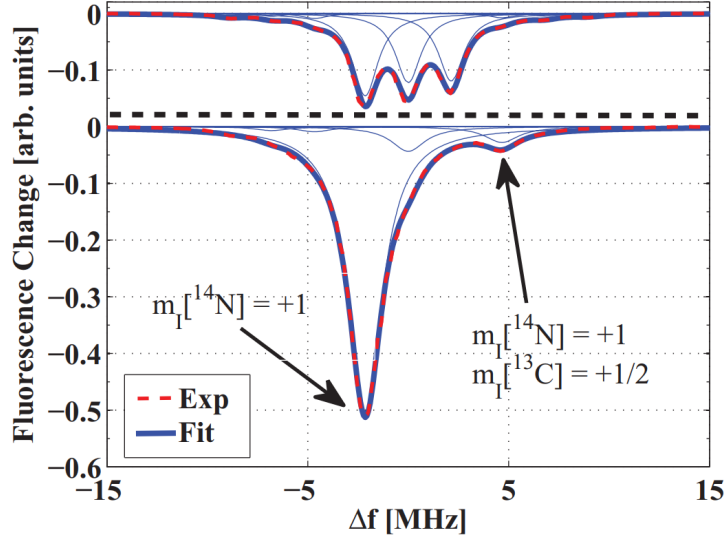
blad equation

Figure 4.5: Top figure: ODMR signal at 21 G. Bottom figure: ODMR signal near the ESLAC at 387 G. Thick dashed curve correspond to the experimental results, thick full curve correspond to the fitted multiple resonances. Narrow curves correspond to the fitted individual resonances. The high peak marked with an arrow corresponds to the ($m_S = 0$, $^{14N}m_I = +1 \to m_S = +1$, $^{14N}m_I = +1$) transition. The marked low peak corresponds to ($m_S = 0$, $m_I[^{14}N] = +1$, $m_I[^{13}C] = +1/2 \to m_S = +1$, $m_I[^{14}N] = +1$, $m_I[^{13}C] = +1/2$) transition, and it is due to hyperfine interaction with 14N and 13C nuclear spins.[20]
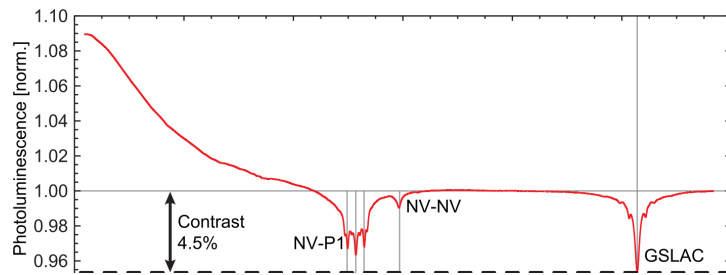

Figure 4.6: NV-PL as a function of the applied MF normalized to the PL at 80 mT

$$\frac{\partial}{\partial t}\rho = -\frac{i}{\hbar}[H, \rho] + L\rho = 0 \qquad (4.4)$$

where ρ is the density matrix of the NV center ^3E state and the ^{14}N nuclear spin. TheLindblad superoperator is written as a sum of all relaxation

$$L\rho = \sum_n \gamma_n \left(C_n \rho C_n^\dagger - \frac{1}{2} C_n C_n^\dagger \rho - \frac{1}{2} \rho C_n C_n^\dagger \right) \qquad (4.5)$$

where γ_n are the decay rates associated with the relaxation processes, and C_n are the Lindblad operators which determine the relaxation process. Here we consider T1 relaxation, T2 relaxation and optical pumping. The C_n operator for T1 is $|i\rangle\langle j|$, leading to a decay of population from state $|j\rangle$ into the state $|i\rangle$, while the operator for T2 is $|i\rangle\langle i| - |j\rangle\langle j|$, which relaxes only the coherence terms. The pumping term of $m_S = \pm 1 \rightarrow m_S = 0$ is written as $\gamma_0|0\rangle\langle\pm 1|$, while non spin-conserving transition $m_S = 0 \rightarrow m_S = \pm 1$ is written as $\gamma_{\pm 1}|\pm 1\rangle\langle 0|$. Calibrating $P = \gamma_0/\gamma_{\pm 1}$ to 20 from experiments and taking T1 and T2 from [32], [58], [20] reproduced the experimental results well by the theoretical simulation of 9-level model(Fig 4.7).

We have reproduced the same result by Mathematica(Fig 4.8).

Now we extend it to a more complete 21-level model. As the decay rate inside the singlets, ^1A to $^1E_{1,2}$, is too fast(about 1 ns[59]). The whole system at the electronic spin level could be analysed by a 7-level model(Fig 4.9). Taking the hyperfine structure into consideration, we obtain a 21-level model. The jump operators are written as $L_k = \sqrt{\Gamma_{mn}}|m\rangle\langle n|$. We also introduce the contribution of spin nonconserving radiative processes, the rate of which we evaluated as $\epsilon = 0.01$ of the rate of spin conserving transitions. Setting the transitions and decay rates in Table5, as well as a optical pumping rate same as the decay rate(saturation excitation), [19] reproduced the experimental finds well by the 21-level model.
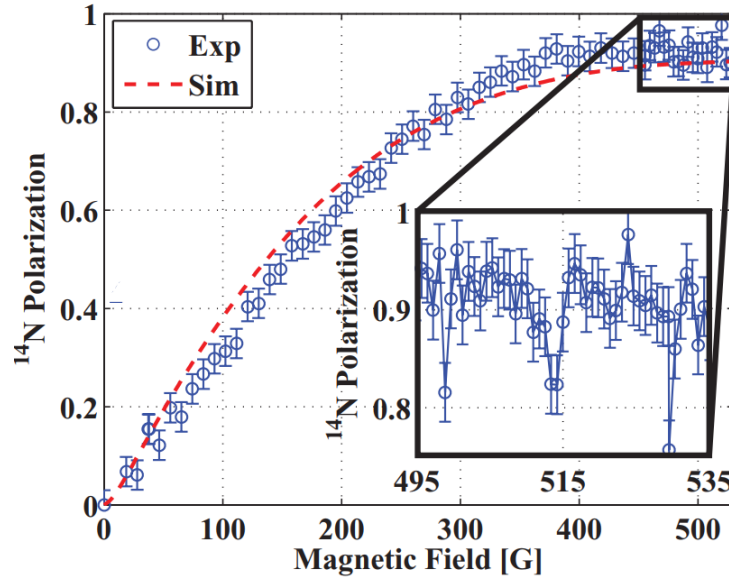
Figure 4.7: Room-temperature 14N nuclear polarization as a function of the axial magnetic field. The circles are the experimental measurements, and the dashed curve is the simulation result at zero strain. Inset: 14N polarization in a narrower magnetic field range showing three dips of the nuclear polarization corresponding to cross-relaxation with P1 centers(not included in the model).
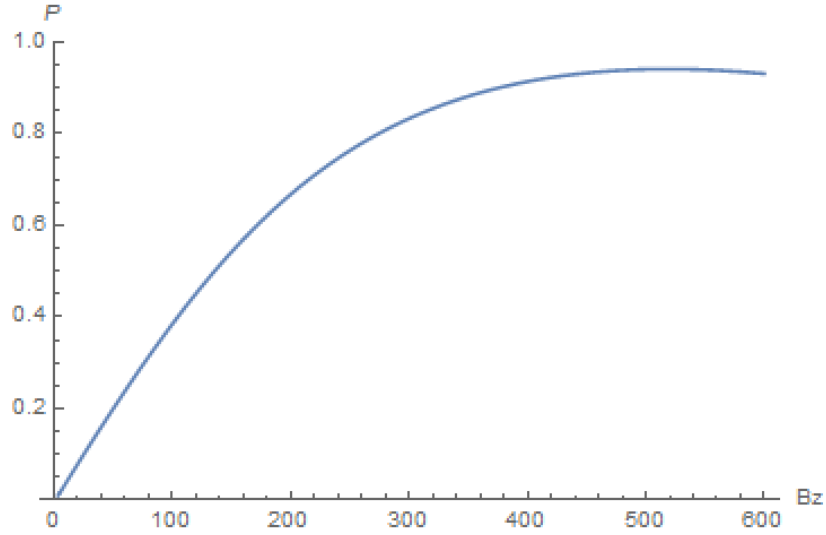

Figure 4.8: Reproduced theoretical calculation of Fig 4.7

Transition		Rate [MHz]
Spontaneous Emission	$\Gamma_{41}, \Gamma_{52}, \Gamma_{63}$	63 ± 3
Intersystem crossing	Γ_{47}	12 ± 3
from ES to singlet	Γ_{57}, Γ_{67}	80 ± 6
Intersystem crossing	Γ_{71}	3.3 ± 0.4
from singlet to GS	Γ_{72}, Γ_{73}	2.4 ± 0.4

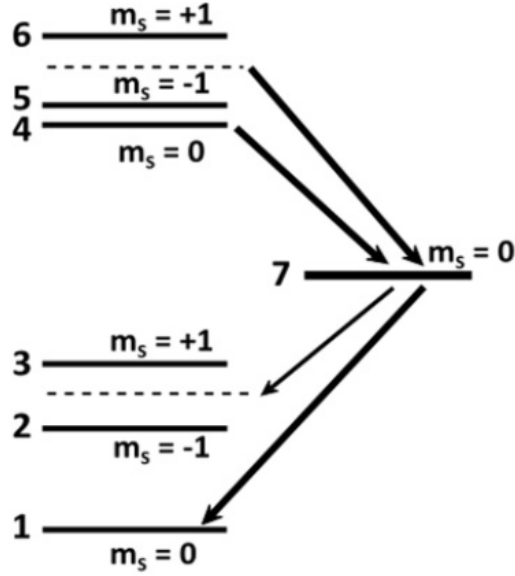Table 5: Transitions and decay rates (from [60]). The labels correspond to the energy levels in Fig. 42

Figure 4.9: Seven-level scheme of the NV electronic structure. Levels 1-3 and 4-6 represent the three different mS projections of the ground and excited state, respectively. Level 7 represents the electronic singlet metastable level.

We reproduce the theoretical results of 21-level model by Mathematica(Fig 4.11).

Since the ODMR signal is mainly from the aligned centers, above analysis works for both the ensemble NV centers[20] and the single NV center[19].
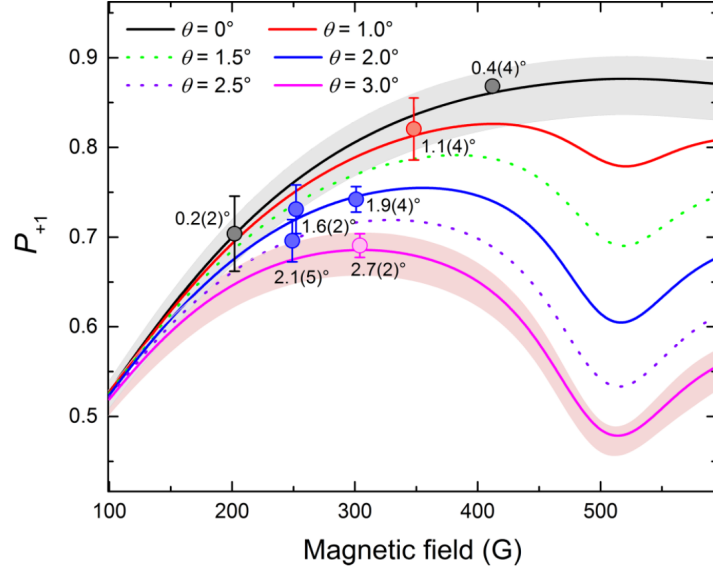
Figure 4.10: Steady-state population P_{+1} of the hyperfine state $|0, +1\rangle_g$ of the magnetic field B for different angles θ with respect to the NV axis. The curves are numerical solutions of the generalized Liouville equation ($\theta = 0.0°, 1.0°, 1.5°, 2.0°, 2.5°,$ and $3.0°$). For the $\theta = 0°, 3°$ lines, the shaded area represents the error due to the uncertainty in the decay rates reported in Table 5 (assume similar uncertainties for the other angles). Circles are experimental results
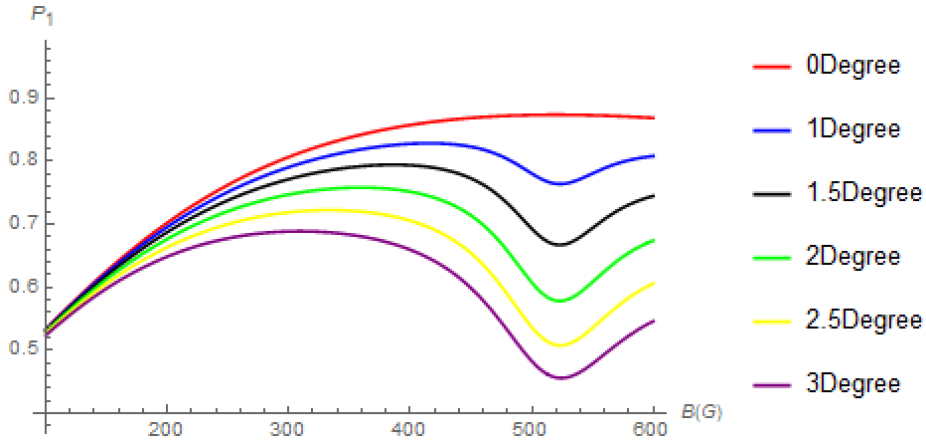

Figure 4.11: Reproduction of the theoretical calculations in Fig 4.10

4.3   Discussion of LAC

Normally, if we scan the magnetic field(no microwave field) and measure photoluminescence, we often could not observe a clear ESLAC dip at good alignment, but could see a GSLAC dip (see Fig 4.6)[21], [61]. One persuasive reason for the GSLAC dip(Fig 4.6) is the low frequency noises. Although seemingly, if we polarize the nuclear spin, there should be no mixing and thus no dip. However, the noise at the splitting frequency, such as 1/f noise or weakly coupled 13C defects may cause the dip, as it induces spin flips into states that do have spin mixing[49]. Then one may wonder, what is the difference between ESLAC and GSLAC? The reason that affects the GSLAC and not the ESLAC is the time scales of the interactions versus the time in the correct state. For the GSLAC, the NV center is on resonance with the low frequency noise unless we add optical pumping. While for the ESLAC, the NV center is only on resonance with the low frequency noise when it is in the excited state, which is on the order of nanoseconds when pumping. To induce a flip from NV-nuclear spin noise it takes several microseconds and similar for the transverse magnetic field. So it is just not in the correct state for long enough to observe the flipping(Dr. David Broadway is greatly appreciated here for email discussion of the GSLAC details in [49]). At ESLAC, the nuclear spin could be polarized is because the off-axial hyperfine interaction $A_\perp$ is greater than the excited-state decay rate of $\sim 1/10\text{ns}^{-1}$[20].

Excepted for the reason mentioned above, we guess that the earth magnetic field may also be a reason for the GSLAC dip, which provides a transverse magnetic field of the same order as the "residual magentic field" in [49].

Here we propose an experimental plan. We can extract the nuclear polarization from the all-optical GSLAC dip, and compare it with the result of ODMR. This two results should be the same. In [52], we can see that

the GSLAC dip is anisotropic for the transverse magnetic field which imply there maybe some coupling of $C13$ which is also anisotropic. A more complete model including C13 and the possible low frequency noise(Markov noise?), extended from the previous 21-level model, could help analyse the GSLAC dip quantitatively.

4.4 Scheme and analysis for room temperature EIT

Before we fully dive into the analysis of room temperature EIT. We first analysis the hyperfine structure at ESLAC again. We calculate the coefficients of the eigenstates of hyperfine structure in Fig 4.3. The results are shown in Fig 4.12.
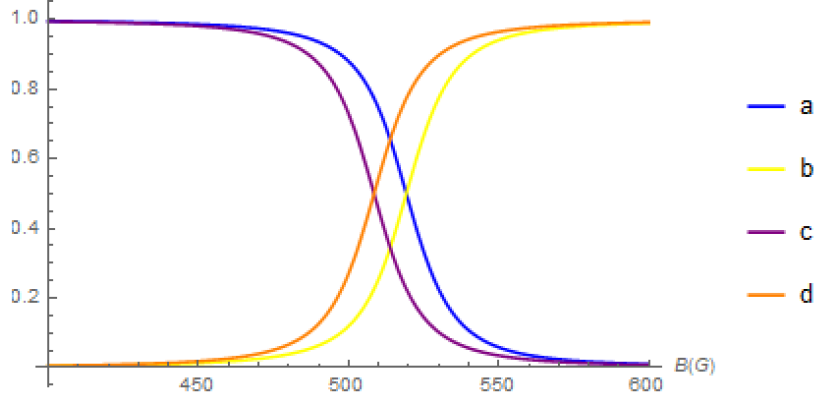
Figure 4.12: Coefficients in Fig 4.3, with four eigenstates $a|0,0\rangle + b|-1,1\rangle, b|0,0\rangle - a|-1,1\rangle, c|0,-1\rangle + d|-1,0\rangle, d|0,-1\rangle - c|-1,0\rangle$

Different from the low temperature CPT and EIT, in the room temperature there is no simple three-level Λ structure. At low temperature, the excited states separate each other about the order of GHz, which make them distinguishable in ZPL. In Fig 3.11(b) and (c)[39], we can see that different

excited states are separated from each other about an order large than the width of the transmission dip, which means: if two excited states interlace, we can use red light at ZPL to resonate exactly the ground states and this superposition state. However, at room temperature, the width of ZPL is much larger than the size of hyperfine structure which is about the order of MHz. Thus, at room temperature, the red light may excite the ground states to all the four superposition states in Fig 4.3.

So now the situation could be approximated to Fig 4.13(here we only consider the case of two photon detuning, neglect the cross excitation as each laser could excite all the states which may also be an important reason if we could not observe EIT in the experiment):
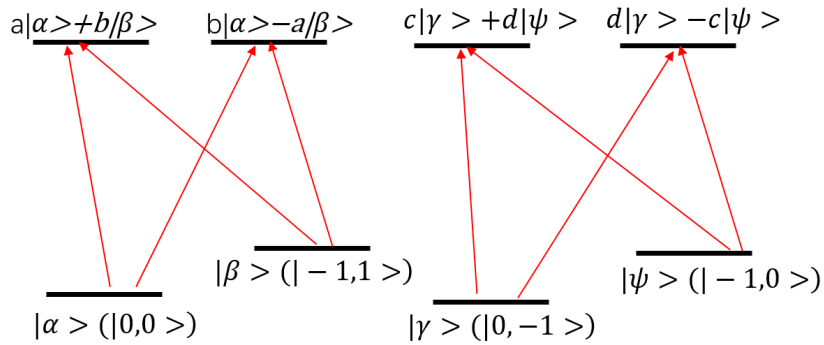

Figure 4.13: This is a simplified model, we assume a wide ZPL would allow the red lights to excite the different Λ structure. It may excite $|0,0\rangle$ and $|-1,1\rangle$ of the ground states to both $a|0,0\rangle + b|-1,1\rangle$ and $b|0,0\rangle - a|-1,1\rangle$ of the excited states with nearly equal probability.

If we adopt this simplified model, then we will find that at the two-photon resonance, there should be no transmission maximum. The reason is that if the ground states are pumped to the dark state of one superposition state, then for another superposition state, it is in its "light state"! The destructive interference will be replaced with a "constructive interference" and will result in an absorption peak rather a transmission peak, which is also supported

by our Mathematica calculation.

So now, it seems that room temperature EIT is not possible and seems very frustrating. But however, the effect of the red light may not work the same for the two different superposition states. And the whole system could not be fully coherent. Our calculation shows that if under proper laser detuning, the excitation of the ground states to each two "dual" superposition states are different, then we will still see a Λ structure, as shown in Fig 4.14.
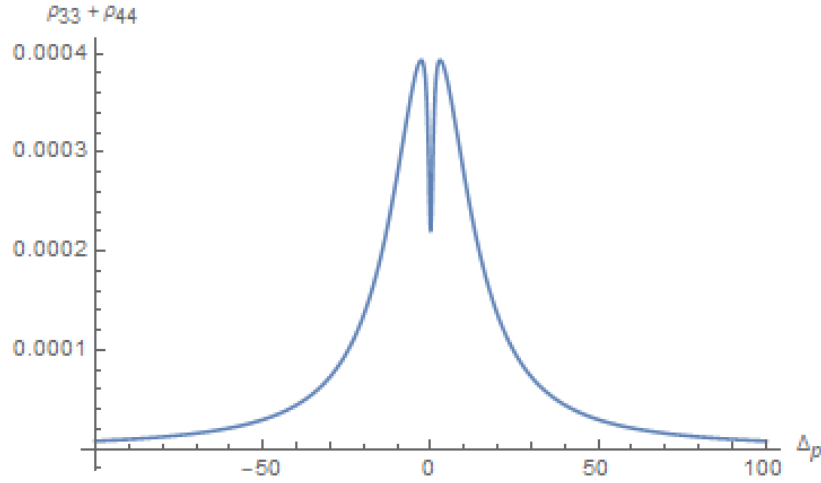

Figure 4.14: The situation when red light is 2.5 times more coupled to one superposition state than to the other. If the ground states are equally excited to the excited superposition states shown in Fig 4.13, there should be only one absorption peak. The parameters are set artificially. The real parameters need to be fit from the experiment.

Above shows the one possibility that we could find something interesting. We know that if there exist a "dark state", then all the population will be pumped to this states. And those intersystem crossing and other states such as states with electronic spin number +1 should not matter. However, due to nuclear and spin polarization and decoherence, some population will inevitably be in $|0, +1\rangle$. Under a transverse magnetic field with frequency resonant between the excited states, the excited state $|0, +1 >$ will be coupled

with $|-1, +1 >$, which is coupled with $|0, 0 >$ by hyperfine interaction. So we may also observe something interesting with a microwave resonant between the hyperfine excited states. If we could observe EIT, then the sensitivity to magnetic fields could be calculated by Eq. (4.6), where P is the detected optical power, E_p is the photon energy, and t_m is the measurement time, R_1 is the EIT contrast, $\Delta\nu_{\text{EIT}}$ is FWHM of EIT.

$$\delta B_{\min} \simeq \frac{1}{g\mu_B \cos\theta} \frac{\Delta\nu_{\text{EIT}}}{R_1} \sqrt{\frac{E_p}{Pt_m}} \qquad (4.6)$$

Now we discuss the possible experimental scheme. The first important thing is to try to narrow ZPL(or find a not so bad ZPL peak) to distinguish the different hyperfine eigenstates(A complete distinction is not possible, this needs a ZPL of at most 0.1GHZ). Then we can just use two red light at ZPL with a frequency difference the same as the frequency difference of the two ground states. The detuning from ZPL should be optimized to find a best EIT contrast. In order to avoid the photon bleaching as 637nm light will pump the NV center to a dark state[62], we need to alternate green and red pulses[17]. The rate of photon bleaching should be much slower than the building time of EIT.

Then, we can use a radiofrequency π pulse ($t_\pi \sim 30\mu$s) on resonance with the $|0, +1\rangle_g \leftrightarrow |0, 0\rangle_g$, to coherently reverses the population of nuclear spin projections $m_I = 0, +1$and alters polarization. This may shorten the building time of EIT. A very similar case in room temperature is shown in Fig 4.15. The most significant advantage of this low temperature Λ structure is that the polarization photon will be entangled with the solid state and thus create a Bell state(Eq 4.7)[39]. However, at room temperature, the polarization is mixed and there is not entanglement. But it is possible to realize quantum memory in the intrinsic nitrogen nuclear spin using Landau-Zener transitions[63].

$$|A_2\rangle = \frac{1}{\sqrt{2}} \left(|E_-\rangle\,|+1\rangle + |E_+\rangle\,|-1\rangle \right) \tag{4.7}$$

Besides, we can test the effect of the microwave resonant between the hyperfine excited states and try CPT with different excitation intensity ratio.

For the scheme in the low temperature, we guess that distinguishing the two excitation light(avoid phonon-induced cross excitation) by polarizing them may improve the contrast of low temperature EIT in [17].
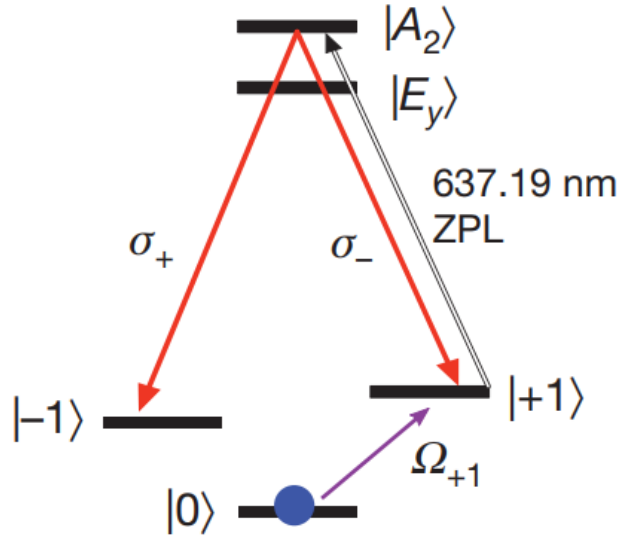

Figure 4.15: Scheme for spin-photon entanglement in the low temperature: Following selective excitation to the $|A_2\rangle$ state, the Λ-type three level system decays to two different spin states through the emission of orthogonally polarized photons, resulting in spin-photon entanglement.

Chapter 5

Conclusion

5.1 Conclusion

This report reviews the past knowledge of EIT and the NV center and tries to cover the background knowledge needed for future realization of NV EIT at room temperature. We first investigated the basic physics of the general EIT and the NV center in detail. Then we started from the previous NV EIT at low temperature which will provide a practical reference for the realization of NV EIT at room temperature. Then we concluded the main principles of GSLAC and ESLAC and reproduced many related results. Finally we analysis the difficulties and the hope of room temperature NV EIT. We conclude that room temperature NV EIT maybe not possible using the ESLAC because the wide ZPL could bring about the excitation of all Λ structure. However, there is still little hope due to the possible incongruity of different Λ structure. The previous coherent manipulations of NV center in room temperature focused on using microwave between the ground states. In our knowledge, the endeavour for the realization of room temperature EIT, even not successful, may provide some important results as the first quantum optics study using resonant excitation in the room temperature NV center.

Bibliography

[1] K-J Boller, A Imamoğlu, and Stephen E Harris. Observation of electromagnetically induced transparency. *Physical Review Letters*, 66(20):2593, 1991.

[2] Marlan O Scully and M Suhail Zubairy. Quantum optics, 1999.

[3] Ralf Röhlsberger, Hans-Christian Wille, Kai Schlage, and Balaram Sahoo. Electromagnetically induced transparency with resonant nuclei in a cavity. *Nature*, 482(7384):199, 2012.

[4] Lene Vestergaard Hau, Stephen E Harris, Zachary Dutton, and Cyrus H Behroozi. Light speed reduction to 17 metres per second in an ultracold atomic gas. *Nature*, 397(6720):594, 1999.

[5] D Budker, DF Kimball, SM Rochester, and VV Yashchuk. Nonlinear magneto-optics and reduced group velocity of light in atomic vapor with slow ground state relaxation. *Physical review letters*, 83(9):1767, 1999.

[6] Robin Santra, Ennio Arimondo, Tetsuya Ido, Chris H Greene, and Jun Ye. High-accuracy optical clock via three-level coherence in neutral bosonic sr 88. *Physical Review Letters*, 94(17):173002, 2005.

[7] SE Harris and Lene Vestergaard Hau. Nonlinear optics at low light levels. *Physical Review Letters*, 82(23):4611, 1999.

[8] Magnus Albert, Aurélien Dantan, and Michael Drewsen. Cavity electromagnetically induced transparency and all-optical switching using ion coulomb crystals. *Nature Photonics*, 5(10):633, 2011.

[9] Jonathan P Marangos. Electromagnetically induced transparency. *Journal of Modern Optics*, 45(3):471–503, 1998.

[10] Michael Fleischhauer, Atac Imamoglu, and Jonathan P Marangos. Electromagnetically induced transparency: Optics in coherent media. *Reviews of modern physics*, 77(2):633, 2005.

[11] BB Buckley, GD Fuchs, LC Bassett, and DD Awschalom. Spin-light coherence for single-spin measurement and control in diamond. *Science*, 330(6008):1212–1215, 2010.

[12] Nir Bar-Gill, Linh M Pham, Andrejs Jarmola, Dmitry Budker, and Ronald L Walsworth. Solid-state electronic spin coherence time approaching one second. *Nature communications*, 4:1743, 2013.

[13] Charles Santori, David Fattal, Sean M Spillane, Marco Fiorentino, Raymond G Beausoleil, Andrew D Greentree, Paolo Olivero, Martin Draganski, James R Rabeau, Patrick Reichart, et al. Coherent population trapping in diamond nv centers at zero magnetic field. *Optics Express*, 14(17):7986–7994, 2006.

[14] Charles Santori, Philippe Tamarat, Philipp Neumann, Jörg Wrachtrup, David Fattal, Raymond G Beausoleil, James Rabeau, Paolo Olivero, Andrew D Greentree, Steven Prawer, et al. Coherent population trapping of single spins in diamond under optical excitation. *Physical review letters*, 97(24):247401, 2006.

[15] Christopher G Yale, Bob B Buckley, David J Christle, Guido Burkard, F Joseph Heremans, Lee C Bassett, and David D Awschalom. All-optical control of a solid-state spin using coherent dark states. *Proceedings of the National Academy of Sciences*, 110(19):7595–7600, 2013.

[16] PR Hemmer, AV Turukhin, MS Shahriar, and JA Musser. Raman-excited spin coherences in nitrogen-vacancy color centers in diamond. *Optics Letters*, 26(6):361–363, 2001.

[17] Victor M Acosta, Kasper Jensen, Charles Santori, Dmitry Budker, and Rymond G Beausoleil. Electromagnetically induced transparency in a diamond spin ensemble enables all-optical electromagnetic field sensing. *Physical review letters*, 110(21):213605, 2013.

[18] A Batalov, V Jacques, F Kaiser, P Siyushev, P Neumann, LJ Rogers, RL McMurtrie, NB Manson, F Jelezko, and J Wrachtrup. Low temperature studies of the excited-state structure of negatively charged nitrogen-vacancy color centers in diamond. *Physical review letters*, 102(19):195506, 2009.

[19] F Poggiali, P Cappellaro, and N Fabbri. Measurement of the excited-state transverse hyperfine coupling in nv centers via dynamic nuclear polarization. *Physical Review B*, 95(19):195308, 2017.

[20] Ran Fischer, Andrey Jarmola, Pauli Kehayias, and Dmitry Budker. Optical polarization of nuclear ensembles in diamond. *Physical Review B*, 87(12):125207, 2013.

[21] LJ Rogers, RL McMurtrie, MJ Sellars, and NB Manson. Time-averaging within the excited state of the nitrogen-vacancy centre in diamond. *New Journal of Physics*, 11(6):063007, 2009.

[22] V Jacques, P Neumann, J Beck, M Markham, D Twitchen, J Meijer, F Kaiser, G Balasubramanian, F Jelezko, and J Wrachtrup. Dynamic polarization of single nuclear spins by optical pumping of nitrogen-vacancy color centers in diamond at room temperature. *Physical review letters*, 102(5):057403, 2009.

[23] Dmitry Budker, Derek F Kimball, Derek Kimball, and David P DeMille. *Atomic physics: an exploration through problems and solutions*. Oxford University Press, USA, 2004.

[24] Maximilian A Schlosshauer. *Decoherence: and the quantum-to-classical transition*. Springer Science & Business Media, 2007.

[25] A Imamoğlu and Stephen E Harris. Lasers without inversion: interference of dressed lifetime-broadened states. *Optics letters*, 14(24):1344–1346, 1989.

[26] Tony Y Abi-Salloum. Electromagnetically induced transparency and autler-townes splitting: Two similar but distinct phenomena in two categories of three-level atomic systems. *Physical Review A*, 81(5):053836, 2010.

[27] Maximilian A Schlosshauer. *Decoherence: and the quantum-to-classical transition*. Springer Science & Business Media, 2007.

[28] Marcus W Doherty, Neil B Manson, Paul Delaney, Fedor Jelezko, Jörg Wrachtrup, and Lloyd CL Hollenberg. The nitrogen-vacancy colour centre in diamond. *Physics Reports*, 528(1):1–45, 2013.

[29] JHN Loubser and JA Van Wyk. Electron spin resonance in annealed type 1b diamond. *Diamond Res*, 11:4–7, 1977.

[30] JoHoNo Loubser and JoA van Wyk. Electron spin resonance in the study of diamond. *Reports on Progress in Physics*, 41(8):1201, 1978.

[31] Jeronimo R Maze, Adam Gali, Emre Togan, Yiwen Chu, Alexei Trifonov, Efthimios Kaxiras, and Mikhail D Lukin. Properties of nitrogen-vacancy centers in diamond: the group theoretic approach. *New Journal of Physics*, 13(2):025025, 2011.

[32] NB Manson, JP Harrison, and MJ Sellars. Nitrogen-vacancy center in diamond: Model of the electronic structure and associated dynamics. *Physical Review B*, 74(10):104303, 2006.

[33] Marcus W Doherty, Neil B Manson, Paul Delaney, and Lloyd CL Hollenberg. The negatively charged nitrogen-vacancy centre in diamond: the electronic solution. *New Journal of Physics*, 13(2):025019, 2011.

[34] A Lenef and SC Rand. Electronic structure of the n-v center in diamond: Theory. *Physical Review B*, 53(20):13441, 1996.

[35] P Siyushev, H Pinto, M Vörös, A Gali, Fedor Jelezko, and J Wrachtrup. Optically controlled switching of the charge state of a single nitrogen-vacancy center in diamond at cryogenic temperatures. *Physical review letters*, 110(16):167402, 2013.

[36] Yuchen Ma, Michael Rohlfing, and Adam Gali. Excited states of the negatively charged nitrogen-vacancy color center in diamond. *Physical Review B*, 81(4):041204, 2010.

[37] Neil Manson, Lachlan Rogers, Marcus Doherty, and Lloyd Hollenberg. Optically induced spin polarisation of the nv-centre in diamond: role of electron-vibration interaction. *arXiv preprint arXiv:1011.2840*, 2010.

[38] Marcus W Doherty, Neil B Manson, Paul Delaney, and Lloyd CL Hollenberg. The negatively charged nitrogen-vacancy centre in diamond: the electronic solution. *New Journal of Physics*, 13(2):025019, 2011.

[39] Emre Togan, Yiwen Chu, AS Trifonov, Liang Jiang, Jeronimo Maze, Lilian Childress, MV Gurudev Dutt, Anders Søndberg Sørensen, PR Hemmer, Alexander S Zibrov, et al. Quantum entanglement between an optical photon and a solid-state spin qubit. *Nature*, 466(7307):730, 2010.

[40] A Batalov, V Jacques, F Kaiser, P Siyushev, P Neumann, LJ Rogers, RL McMurtrie, NB Manson, F Jelezko, and J Wrachtrup. Low temperature studies of the excited-state structure of negatively charged nitrogen-vacancy color centers in diamond. *Physical review letters*, 102(19):195506, 2009.

[41] AT Collins, MF Thomaz, and Maria Isabel B Jorge. Luminescence decay time of the 1.945 ev centre in type ib diamond. *Journal of Physics C: Solid State Physics*, 16(11):2177, 1983.

[42] LJ Rogers, RL McMurtrie, MJ Sellars, and NB Manson. Time-averaging within the excited state of the nitrogen-vacancy centre in diamond. *New Journal of Physics*, 11(6):063007, 2009.

[43] Yiwen Chu and Mikhail D Lukin. Quantum optics with nitrogen-vacancy centers in diamond. *Quantum Optics and Nanophotonics; Fabre, C., Sandoghdar, V., Treps, N., Cugliandolo, LF, Eds*, pages 229–270, 2015.

[44] P Jamonneau, G Hétet, A Dréau, J-F Roch, and V Jacques. Coherent population trapping of a single nuclear spin under ambient conditions. *Physical review letters*, 116(4):043603, 2016.

[45] Christopher G Yale, Bob B Buckley, David J Christle, Guido Burkard, F Joseph Heremans, Lee C Bassett, and David D Awschalom. All-optical control of a solid-state spin using coherent dark states. *Proceedings of the National Academy of Sciences*, 110(19):7595–7600, 2013.

[46] MW Doherty, F Dolde, H Fedder, Fedor Jelezko, J Wrachtrup, NB Manson, and LCL Hollenberg. Theory of the ground-state spin of the nv-center in diamond. *Physical Review B*, 85(20):205203, 2012.

[47] S Felton, AM Edmonds, ME Newton, PM Martineau, D Fisher, DJ Twitchen, and JM Baker. Hyperfine interaction in the ground state of the negatively charged nitrogen vacancy center in diamond. *Physical Review B*, 79(7):075203, 2009.

[48] Florian Dolde, Helmut Fedder, Marcus W Doherty, Tobias Nöbauer, Florian Rempp, Gopalakrishnan Balasubramanian, Thomas Wolf, Friedemann Reinhard, Lloyd CL Hollenberg, Fedor Jelezko, et al. Electric-field sensing using single diamond spins. *Nature Physics*, 7(6):459, 2011.

[49] David A Broadway, James DA Wood, Liam T Hall, Alastair Stacey, Matthew Markham, David A Simpson, Jean-Philippe Tetienne, and Lloyd CL Hollenberg. Anticrossing spin dynamics of diamond nitrogen-vacancy centers and all-optical low-frequency magnetometry. *Physical Review Applied*, 6(6):064001, 2016.

[50] Viktor Ivády, Krisztián Szász, Abram L Falk, Paul V Klimov, David J Christle, Erik Janzén, Igor A Abrikosov, David D Awschalom, and Adam Gali. Theoretical model of dynamic spin polarization of nuclei

coupled to paramagnetic point defects in diamond and silicon carbide. *Physical Review B*, 92(11):115206, 2015.

[51] Marcis Auzinsh, Andris Berzins, Dmitry Budker, Laima Busaite, Ruvin Ferber, Florian Gahbauer, Reinis Lazda, Arne Wickenbrock, and Huijie Zheng. Hyperfine level structure in nitrogen-vacancy centers near the ground-state level anticrossing. *Physical Review B*, 100(7):075204, 2019.

[52] Huijie Zheng, Zhiyin Sun, Georgios Chatzidrosos, Chen Zhang, Kazuo Nakamura, Hitoshi Sumiya, Takeshi Ohshima, Junichi Isoya, Jörg Wrachtrup, Arne Wickenbrock, et al. Microwave-free vector magnetometry with nitrogen-vacancy centers along a single axis in diamond. *arXiv preprint arXiv:1904.04361*, 2019.

[53] Arne Wickenbrock, Huijie Zheng, Lykourgos Bougas, Nathan Leefer, Samer Afach, Andrey Jarmola, Victor M Acosta, and Dmitry Budker. Microwave-free magnetometry with nitrogen-vacancy centers in diamond. *Applied Physics Letters*, 109(5):053505, 2016.

[54] Jun John Sakurai and Eugene D Commins. Modern quantum mechanics, revised edition, 1995.

[55] A Dréau, J-R Maze, M Lesik, J-F Roch, and V Jacques. High-resolution spectroscopy of single nv defects coupled with nearby 13 c nuclear spins in diamond. *Physical Review B*, 85(13):134107, 2012.

[56] Hai-Jing Wang, Chang S Shin, Claudia E Avalos, Scott J Seltzer, Dmitry Budker, Alexander Pines, and Vikram S Bajaj. Sensitive magnetic control of ensemble nuclear spin hyperpolarization in diamond. *Nature communications*, 4:1940, 2013.

[57] Benjamin Smeltzer, Lilian Childress, and Adam Gali. 13c hyperfine interactions in the nitrogen-vacancy centre in diamond. *New Journal of Physics*, 13(2):025021, 2011.

[58] Philipp Neumann, Johannes Beck, Matthias Steiner, Florian Rempp, Helmut Fedder, Philip R Hemmer, Jörg Wrachtrup, and Fedor Jelezko. Single-shot readout of a single nuclear spin. *Science*, 329(5991):542–544, 2010.

[59] JP Tetienne, L Rondin, P Spinicelli, M Chipaux, T Debuisschert, JF Roch, and V Jacques. Magnetic-field-dependent photodynamics of single nv defects in diamond: an application to qualitative all-optical magnetic imaging. *New Journal of Physics*, 14(10):103033, 2012.

[60] Lucio Robledo, Hannes Bernien, Toeno Van Der Sar, and Ronald Hanson. Spin dynamics in the optical cycle of single nitrogen-vacancy centres in diamond. *New Journal of Physics*, 13(2):025013, 2011.

[61] RJ Epstein, FM Mendoza, YK Kato, and DD Awschalom. Anisotropic interactions of a single spin and dark-spin spectroscopy in diamond. *Nature physics*, 1(2):94, 2005.

[62] Katja Beha, Anton Batalov, Neil B Manson, Rudolf Bratschitsch, and Alfred Leitenstorfer. Optimum photoluminescence excitation and recharging cycle of single nitrogen-vacancy centers in ultrapure diamond. *Physical review letters*, 109(9):097404, 2012.

[63] GD Fuchs, Guido Burkard, PV Klimov, and DD Awschalom. A quantum memory intrinsic to single nitrogen–vacancy centres in diamond. *Nature Physics*, 7(10):789, 2011.